This is a Just Accepted version, keep updated with https://doi.org/10.26599/OCEAN.2026.9470035

OCEAN 2026, 2, 9470035

Research Article

https://doi.org/10.26599/OCEAN.2026.9470035

Non-monotonic effects of surface slip on hydrofoil noise at zero angle of attack: Trade-off between drag reduction and noise mitigation under large slip lengths

Manfu Zhu[1], Hongbo Huang[2], Nan Zhang[2], Weixi Huang[3,4], Liran Ma[1,5,*], Jianbin Luo[1,5,*]

[1] *Department of Mechanical Engineering, Tsinghua University, Beijing 100084, China*

[2] *China Ship Scientific Research Center, Wuxi 214082, China*

[3] *AML, Department of Engineering Mechanics, Tsinghua University, Beijing 100084, China*

[4] *State Key Laboratory of Advanced Space Propulsion, Tsinghua University, Beijing 100084, China*

[5] *State Key Laboratory of Tribology in Advanced Equipment, Tsinghua University, Beijing 100084, China*

Address correspondence to Liran Ma, maliran@tsinghua.edu.cn; Jianbin Luo, luojb@mail.tsinghua.edu.cn

Received: July 1, 2026 / Revised: November 6, 2026 / Accepted: November 10, 2026

Just Accepted

ABSTRACT

Surface slip has shown significant flow control effects on drag reduction and flow field manipulation. However, the slip effects on flow noise characteristics have not been fully understood. In the present study, a wide range of slip lengths (10–500 μm) are applied on a NACA 0012 hydrofoil surface to investigate the slip effects on the hydrofoil flow noise performance at Reynolds number of 3.6×10^5 and zero angle of attack using large eddy

simulation coupled with the Ffowcs Williams–Hawkings acoustic analogy. Surface slip has been found to push the flow back to the laminar state, thereby significantly reducing the hydrofoil drag and flow noise. However, slip can also trigger flow separation and enhance the bluntness effect at the hydrofoil trailing edge, thereby inducing stronger tonal noise and enhanced pressure fluctuations. Consequently, the overall noise demonstrates a non-monotonic variation in a decrease–increase–decrease–increase trend as slip length increases. Flow maps under different slip lengths are further provided. This work suggests that surface slip does not necessarily reduce the flow noise, but instead presents a trade-off between drag reduction and noise mitigation under large slip lengths, which can provide valuable insights for practical applications of slippery materials in ocean engineering.

Keywords: hydrofoil; surface slip; flow noise; non-monotonic; large eddy simulation

1 Introduction

Underwater radiated noise from surface ships and underwater vehicles has become a critical concern in ocean engineering, affecting marine ecosystem, sonar performance, and passenger comfort [1-4]. As hydrofoils serve as fundamental elements including propeller blades and rudders, mitigating the flow noise of hydrofoils is essential for the acoustic performance of surface ships and underwater vehicles [5, 6]. In addition, as ships and underwater vehicles are advancing towards higher speed and longer cruising range, it is of equal importance to enhance the hydrodynamic performance as well to ensure excellent overall performance [5, 7]. To achieve this goal, various flow control methods have been developed nowadays, which can be classified into active methods and passive methods. Active methods such as gas/polymer injection [8] and traveling waves [9] have demonstrated significant flow control effects. However, they often rely on external energy and mass supply, which typically suffer from the problem of obtaining net energy gains and increasing the complexity in practical implementation. Passive control methods such as riblets [10,

Just Accepted

11], superhydrophobic surfaces [12-15], slippery liquid-infused surfaces [16-18], porous materials [19, 20], and bio-inspired leading edge waviness and trailing edge serrations [6, 21, 22] have also demonstrated remarkable flow control effects and gained significant interest to both the scientific and engineering communities due to the advantages in implementation convenience.

Among these passive control techniques, superhydrophobic surfaces characterized by a large water contact angle (>150°) and low contact angle hysteresis have drawn extensive attention due to the dramatic drag reduction and flow control effects in both laminar and turbulent flow regimes [23, 24]. Compared to the widely explored trailing edge serrations, the superhydrophobic surfaces possess special advantages in flow control. The trailing edge serrations inspired by the silent flight of owls are mainly designed for noise control, in that they can break up the turbulent vortices at the trailing edge, lead to spanwise decoherence and phase interference of noise emission, and thereby reduce the trailing edge noise [25-27]. However, significant flow control effects apart from noise reduction can be obtained by superhydrophobic surfaces, such as drag reduction, flow separation suppression, and flow transition delay. The flow control effects of superhydrophobic surfaces are mainly attributed to the large effective slip at the solid-liquid interfaces due to the presence of a thin air layer formed between water and the solid surface. The surface slip can be vividly illustrated by the slip length model proposed by Navier [28] in 1823. As shown in Fig. 1, compared with the no-slip boundary condition, there exists a slip velocity (U_s) at the solid-liquid interface in the slip length model, and the slip velocity is linearly proportional to the shear rate at the interface in the form of $U_s = L_s\,(\partial u/\partial y)$, where L_s is the slip length, representing the distance below the interface where the surface velocity extrapolates linearly to zero. It can be found that compared to the no-slip case, surface slip can significantly reduce near wall velocity gradient, influence the generation of the boundary layer, and affect the macroscopic flow field. Therefore, surface slip is considered as one of the most effective strategies for flow control in managing the

Just Accepted

generation of boundary layer, compared to the methods that modify the already formed boundary layer [29]. Various experimental measurements have demonstrated that slip lengths on superhydrophobic surfaces can reach hundreds of micrometers, as shown in Table S1 in the Electronic Supplementary Material (ESM) [30-32], which is considered sufficient to influence the macroscopic performance.

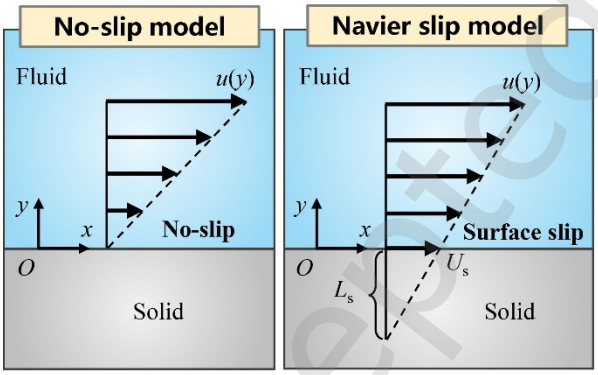


Figure 1 Illustration of the no-slip and slip boundary conditions at the solid-liquid interface.

Despite the simplicity of the homogeneous Navier slip model, the practical superhydrophobic surfaces are usually heterogeneous with mixed liquid-gas slip interfaces and solid-liquid no-slip interfaces, the adaptability of using Navier slip model to represent the physical superhydrophobic surfaces still needs to be examined. Apart from the Navier slip model, there exists a heterogeneous model with alternating slip and no-slip boundary conditions to represent the superhydrophobic surface textures. Martell et al.[33, 34] adopted the heterogeneous model with alternating slip and no-slip boundary conditions to represent the liquid-gas interface and the solid surface, respectively. They found that the superhydrophobic surface reduces the turbulent drag mainly by manipulating the laminar sublayer in the bottom of the boundary layer, and the mean velocity profile is shifted upward with a slip velocity offset that increases with the microstructure spacing. Turk et al.[35] investigated the effects of superhydrophobic surfaces using the alternating slip and no-slip boundary conditions. They found that the increase of the bulk mean velocity is mainly governed

Just Accepted

by the effective slip length, and they have proposed a simple model estimating the gain due to superhydrophobic surfaces in turbulent flows at high Reynolds numbers. A series of follow-up direct numerical simulations performed by Seo and Mani[36], Seo et al.[37], Fairhall et al.[38] and Xie et al.[39] validated the effectiveness of the homogeneous Navier slip length model in representing the superhydrophobic surface with surface textures and heterogeneous slip properties. Results showed that for texture sizes as large as $L^+ \leq 25$ (L^+ is the texture pattern spacing in wall unit), the superhydrophobic surface and the effects of the texture can be well modeled with the homogeneous slip boundary condition, even when the liquid-gas interfacial dynamics effect on the textured surface is taken into account. Therefore, the homogeneous Navier slip length model provides an effective and accurate approach for simulating superhydrophobic surfaces, and it can be used in most laminar and turbulent flow conditions with significantly reduced complexity and computational cost.

Due to the large effective slip lengths, significant flow control effects have been achieved on superhydrophobic surfaces for both internal and external flows, including the flow around the hydrofoil. For instance, Gogte et al. [40] obtained up to 18% drag reduction on a Joukovsky hydrofoil with a superhydrophobic coating at Reynolds number (Re) of 1500. Lee et al. [41] found that the superhydrophobic coating can either induce early vortex rollup or slightly delayed vortex rollup of a NACA 0012 hydrofoil depending on the angle of attack at $\mathrm{Re} = 0.2\times10^4 - 1.0\times10^4$. Sooraj et al. [42] found that the superhydrophobic coating can delay flow separation and increase the stall angle of a NACA 0015 hydrofoil, and up to 40% drag reduction has been achieved at angle of attack of 15° and Re = 30800, with root mean square (rms) lift coefficient reduced as well. Mallah et al. [43] found that the superhydrophobic surface can have significant effects on a pitching NACA 0012 foil for Strouhal number (St) of 0.08–0.65 at Re = 2400, with lift coefficient enhanced at low St. Numerical simulations have also been carried out to investigate the effects and

Just Accepted

underlying mechanisms of surface slip on the hydrofoil performance across ultra-low, low, moderate, and high Re range of Re = $\boldsymbol{O}$ (10^3–10^7) [29, 44-46], and much more complex effects of surface slip on the hydrodynamic performance have been discovered. For example, Shahsavari et al. [47] found an unexpected hydrofoil lift coefficient decrease phenomenon for slip cases at Re = 1.0×10^5. They found that surface slip can induce non-attached flow separation near the hydrofoil trailing edge, which significantly reduces the pressure difference on the hydrofoil surface and decreases the lift coefficient. Zhu et al. [48] found that apart from the drag reduction effect, surface slip can also induce drag increase phenomena of the hydrofoil, and this drag increase phenomena occur at relatively large angles of attack (6°–10°) with small slip lengths (≤50 μm) when slip is applied only on the pressure side of the hydrofoil.

Despite the extensive studies on the hydrodynamic performance, impacts of surface slip on hydrofoil flow noise characteristics remain largely unexplored. For geometries like the cylinder and the flat plate, several previous works have been carried out. Niu et al. [49] numerically found that the superhydrophobic surface can effectively reduce the flow-induced noise and change the sound radiation directivity of a circular cylinder by controlling vortex shedding and reducing pressure fluctuations. Barandagh et al. [50] also found that the superhydrophobic surface can reduce the tonal noise and overall noise of the circular cylinder at Re = 3900. Chen et al. [51] experimentally found that the superhydrophobic surface can reduce the near-field hydrodynamic noise of a flat plate at Re = $\boldsymbol{O}$ (10^6) by controlling vortex shedding, stabilizing the flow, and weakening the flow energy. Also, they found that the superhydrophobic plate with lower drag reduction rate demonstrates higher noise mitigation effect, which indicates that there is no monotonic relationship between drag reduction and noise mitigation. The above results have demonstrated the flow noise reduction effects of surface slip on the circular cylinder and the flat plate. However, effects of surface slip on flow noise characteristics of the hydrofoil—a geometry

Just Accepted

directly relevant to marine propellers and rudders for surface ships and underwater vehicles—remain unexplored. As hydrofoils usually experience more complex flow phenomena such as flow separation, transition, and reattachment compared to the cylinder and the flat plate due to the variation in Reynolds number, angle of attack, and surface curvature [52-54], it is therefore imperative to further investigate the effects of surface slip on the hydrofoil flow noise performance. Also, despite the extensive studies investigating the hydrofoil hydrodynamic performance and flow field under surface slip, the results cannot be readily used to predict the hydrofoil flow noise performance, since flow noise performance is not only related to the overall flow state, but also closely related to the specific region where flow transition occurs, whether and where flow separation occurs, and the magnitude of turbulent fluctuations and the vortex shedding strength.

Based on the above considerations, the effects of surface slip on the flow noise characteristics of a NACA 0012 hydrofoil are fully investigated in the present work by large eddy simulation (LES) coupled with the Ffowcs Williams–Hawkings (FW–H) acoustic analogy at a moderate Reynolds number of $Re = 3.6\times10^5$ and zero angle of attack. A wide range of slip lengths (10–500 μm) are applied on the hydrofoil surface to fully understand the effects of slip from small values to large values on both the hydrodynamic and noise performances. Detailed flow field on the hydrofoil surface and local flow field around the hydrofoil trailing edge are examined, and the underlying mechanisms for the non-monotonic flow noise variation are unraveled. Note that the time-averaged lift coefficient of the symmetric NACA 0012 hydrofoil at zero angle of attack is zero, which means that the hydrofoil does not generate lift forces. However, this does not necessarily mean that the investigation on the hydrofoil performance at zero angle of attack is of no practical significance. As mentioned earlier, hydrofoils usually act as rudders for surface ships and underwater vehicles. In practical applications, the vehicles can cruise without changing the forward direction for a sufficiently long time, and there is no need to operate the rudders to generate

Just Accepted

lift forces or turning forces. Therefore, the flow noise performance and drag performance of the hydrofoil under zero angle of attack become quite important for the acoustic stealth performance and fastness of the vehicle under the straight cruising condition. Furthermore, it can be learned that the flow field and noise generation mechanisms of the hydrofoil or the aerofoil can vary with the angle of attack [55-61]. At non-zero angles of attack, the foil can experience strong adverse pressure gradient on the suction side, and flow separation and transition can occur upstream on the suction side and downstream on the pressure side, which can significantly complex the problem [55-57]. Therefore, as a first examination of slip effects on the hydrofoil flow noise performance over a wide range of slip lengths, this work limits the working condition of the NACA 0012 hydrofoil to zero angle of attack. The following results demonstrate that surface slip can impose a non-monotonic variation on the hydrofoil flow noise performance and induce a complex flow field evolution even at zero angle of attack, thus it can be inferred that the slip effects on hydrofoil noise performance at non-zero angles of attack can be much more complex due to the asymmetric flow field and inherently complex noise generation mechanisms, which however need further investigations.

The paper is organized as follows. Section 2 introduces the numerical method in calculating the flow field and flow noise. The implementation of the slip boundary condition is also presented. Section 3 demonstrates detailed results of the hydrodynamic and flow noise performances of the hydrofoil, with detailed flow field analysis around the hydrofoil. Flow maps demonstrating the flow evolution under different slip lengths are further provided in Section 4. Finally, conclusions are drawn in Section 5.

2 Numerical methods

The present work utilizes high-resolution LES to solve the unsteady flow field and the FW–H acoustic analogy to predict the acoustic performance.

Just Accepted

2.1 Governing equations and model validation

The incompressible viscous flow around the NACA 0012 hydrofoil is calculated by solving the three-dimensional Navier–Stokes equations based on the finite volume method. The wall-resolved LES is used to calculate the three-dimensional flow field. The continuity and momentum equations for LES are written as

$$\frac{\partial \bar{u}_i}{\partial x_i} = 0 \tag{1}$$

$$\frac{\partial}{\partial t}(\rho \bar{u}_i) + \frac{\partial}{\partial x_j}(\rho \bar{u}_i \bar{u}_j) = -\frac{\partial \bar{p}}{\partial x_i} + \frac{\partial}{\partial x_j}[\mu (\frac{\partial \bar{u}_i}{\partial x_j} + \frac{\partial \bar{u}_j}{\partial x_i})] - \frac{\partial}{\partial x_j}(\tau_{ij}) \tag{2}$$

where x_i (i = 1, 2, 3) denote the Cartesian coordinates, ($\bar{\cdot}$) represent filtered quantities of large eddies, u_i are the corresponding velocity components, p is the pressure, ρ is the fluid density, μ is the fluid dynamic viscosity, and τ_{ij} are the sub-grid scale stresses defined by $\tau_{ij} = \rho\overline{u_i u_j} - \rho\bar{u}_i\bar{u}_j$. The sub-grid scale stresses are written as

$$\tau_{ij} = \frac{1}{3}\tau_{kk}\delta_{ij} - \mu_t (\frac{\partial \bar{u}_i}{\partial x_j} + \frac{\partial \bar{u}_j}{\partial x_i}) \tag{3}$$

where δ_{ij} is the Kronecker delta function, τ_{kk} is the isotropic part of the sub-grid scale stresses, and μ_t is the sub-grid scale turbulent viscosity.

In the present study, the wall-adapting local eddy-viscosity (WALE) model [62] is adopted in modeling the sub-grid scale turbulent viscosity μ_t due to the advantage that it returns a zero turbulent viscosity for laminar flows and allows the correct treatment for laminar zones in the computational domain. In the WALE model, the sub-grid scale turbulent viscosity μ_t is written as

$$\mu_t = \rho L_f^2 \frac{(S_{ij}^d S_{ij}^d)^{3/2}}{(\tilde{S}_{ij}\tilde{S}_{ij})^{5/2} + (S_{ij}^d S_{ij}^d)^{5/4}} \tag{4}$$

where $S_{ij}^d = \frac{1}{2}(\tilde{g}_{ij}^2 + \tilde{g}_{ji}^2) - \frac{1}{3}\delta_{ij}\tilde{g}_{kk}^2$ and $\tilde{g}_{ij} = \partial\bar{u}_i/\partial x_j$. L_f is the mixing length for sub-grid scales and

Just Accepted

is computed by $L_f = \min(\kappa d, C_w V^{1/3})$, where κ is the von Kármán constant, d is the distance to the closest wall, V is the volume of the computation cell, and C_w is the WALE constant ($C_w = 0.325$).

The acoustic field is obtained by using the FW–H acoustic analogy [63]. The FW–H acoustic analogy is a frequently adopted method in flow noise prediction [64-67], which decouples the propagation of sound from its generation, therefore enabling the separation of the flow solution process from the acoustics analysis. The far-field noise of the hydrofoil can be obtained by calculating the FW–H equations

$$\frac{1}{c_0^2}\frac{\partial^2 p'}{\partial t^2} - \nabla^2 p' = \frac{\partial^2}{\partial x_i \partial x_j}[T_{ij}H(f)] - \frac{\partial}{\partial x_i}\{[P_{ij}n_i + \rho u_i(u_n - v_n)]\delta(f)\} + \frac{\partial}{\partial t}\{[\rho_0 v_n + \rho(u_n - v_n)]\delta(f)\} \quad (5)$$

where $p' = p - p_0$ is the sound pressure at far field, c_0 is the far-field sound speed ($c_0 = 340$ m/s in air, and $c_0 = 1500$ m/s in water), ρ_0 is the far-field density, P_{ij} is the compressive stress tensor, u_i is the fluid velocity component in the x_i direction, u_n is the fluid velocity component normal to the surface, v_i is the surface velocity component in the x_i direction, v_n is the surface velocity component normal to the surface, $\delta(f)$ is the Dirac delta function, and $H(f)$ is the Heaviside function. $f = 0$ corresponds to the source surface, n_i is the unit normal vector pointing toward the exterior region ($f > 0$). T_{ij} is the Lighthill stress tensor in $T_{ij} = \rho u_i u_j + P_{ij} - c_0^2(\rho - \rho_0)\delta_{ij}$.

The acoustic sources can be obtained by integrating Equation (5). It can be learned from Lighthill [68, 69] that turbulent fluctuations and flow instabilities themselves are inefficient noise radiators in low Mach number flows. Therefore, for the low Mach number incompressible flows, the volume integrals and the quadrupole noise can be neglected. Since the hydrofoil is fixed and rigid, the flow past the hydrofoil does not generate monopole noise. Therefore, only the dipole loading noise p'_L needs to be considered in the present work, which is expressed by

Just Accepted

$$4\pi p'_L(x,t) = \frac{1}{c_0}\int_{f=0}\left[\frac{\dot{L}_r}{r\,(1-M_r)^2}\right]\mathrm{d}S + \int_{f=0}\left[\frac{L_r - L_M}{r^2\,(1-M_r)^2}\right]\mathrm{d}S + \frac{1}{c_0}\int_{f=0}\left[\frac{L_r\{r\dot{M}_r + c_0(M_r - M^2)\}}{r^2\,(1-M_r)^3}\right]\mathrm{d}S \quad (6)$$

where M is the Mach number, $L_r = \vec{L}\cdot\vec{r} = L_i\, r_i$, $U_n = \vec{U}\cdot\vec{n} = U_i\, n_i$, and $\vec{r}$ and $\vec{n}$ denote the unit vectors in the radiation and wall-normal directions, respectively. Furthermore, U_i and L_i can be expressed as

$$U_i = v_i + \frac{\rho}{\rho_0}(u_i - v_i) \quad (7)$$

$$L_i = P_{ij}\,\hat{n}_j + \rho u_i(u_n - v_n) \quad (8)$$

Then, the sound pressure level (SPL) can be expressed as [70]

$$\mathrm{SPL} = 10\,\log\frac{p'^2_L}{p^2_{\mathrm{ref}}} \quad (9)$$

where p_{ref} is the reference sound pressure, and $p_{\mathrm{ref}} = 2\times10^{-5}$ Pa in air, $p_{\mathrm{ref}} = 1\times10^{-6}$ Pa in water.

The overall sound pressure level (OASPL) can then be calculated by

$$\mathrm{OASPL} = 10\,\log\left(\sum_{i=0}^{n} 10^{0.1\,\mathrm{SPL}(f_i)}\right) \quad (10)$$

The benchmark rod–airfoil experiment performed by Jacob et al. [71] is chosen for the current model validation. The experiment was conducted in a large anechoic room. A symmetric NACA 0012 airfoil with chord c = 0.1 m was located one chord downstream of a rod with diameter d = 0.1c, both extending s = 3c in the spanwise direction. Air was supplied by a high-speed subsonic anechoic wind tunnel at a velocity of U = 72 m/s (~0.21 Mach number). The diameter-based Reynolds number of the rod and the chord-based Reynolds number of the airfoil are 4.9×10^4 and 4.9×10^5, respectively. The corresponding numerical settings are established according to the experiment and meshes are constructed, which can be seen from Fig. S1 and Fig. S2 in the ESM. A steady state SST k-ω simulation is firstly performed to ensure a faster convergence for the

Just Accepted

transient simulation. The time-step size for large eddy simulation is set as $\Delta t = 1.0\times10^{-5}$ s [72, 73], and 10000 time-steps are first calculated to ensure a statistically steady flow, with following 10000 time-steps for flow noise calculation and flow statistics sampling. Since the rod and airfoil surfaces are rigid and stationary, and the Mach number is low, the dipole loading noise is expected to dominate the total noise. Therefore, the impermeable rod and airfoil surfaces are selected as the FW–H control surfaces. The sound pressure level at the receiver located 1.85 m above the mid-chord point of the airfoil in the mid-span plane (in line with the experiment) is shown in Fig. 2. It can be found that the predicted spectrum by LES and FW–H method in the present work correlates well with the experimental data obtained by Jacob et al. [71] in both the broadband profile and the tonal peak.

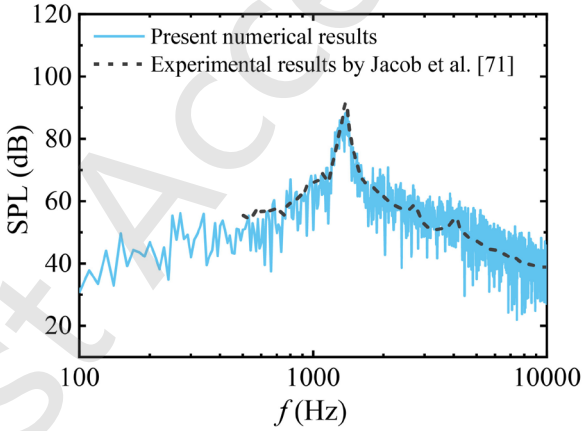


Figure 2 Comparison of the sound pressure level spectra for the rod–airfoil configuration.

The tonal noise characteristics obtained from the experiment and the simulation are further compared in Table 1. It can be found that compared to the permeable surfaces around the rod–airfoil as the FW–H control surfaces adopted by Qin et al. [72], the present simulation adopting the impermeable rod–airfoil surfaces as the FW–H control surfaces also has a high accuracy in capturing the tonal noise frequency and magnitude, which further indicates that for low Mach number flows the dipole noise is the dominant noise, and that the impermeable surfaces can be

Just Accepted

used to obtain high accuracy noise prediction. In addition, the shape, area, and position of the permeable control surfaces can all influence the calculated noise, and improperly selected permeable surfaces can even lead to extra noise and significantly influence the noise results [74]. Therefore, the impermeable surfaces are selected as the FW–H control surfaces for low Mach number flows in the present work due to high accuracy and simplicity. Besides, the OASPL directivity of the rod–airfoil configuration has been checked, as shown in Fig. S3 in the ESM. It can be seen that the predicted acoustic directivity correlates well with the experimental results. Therefore, the above results have demonstrated the accuracy of the LES method and FW–H acoustic analogy in calculating the flow noise performance, which can be used in the following investigations to study the effects of surface slip on the flow noise performance of the NACA 0012 hydrofoil.

Table 1 Comparison of the tonal noise in rod–airfoil configuration.

Results	Frequency (Hz)	SPL (dB)	Error	
			Frequency	SPL (dB)
Experiment [71]	1382.4	91.7	-	-
Present work	1382.8	88.3	0.03%	-3.4
Qin et al. [72]	1375.6	89.1	-0.49%	-2.6

2.2 Numerical settings of NACA 0012 hydrofoil

The numerical settings and mesh generation for the NACA 0012 hydrofoil simulation can be found in Fig. 3. As shown in Fig. 3(a), the coordinate origin is located at the leading edge of the NACA 0012 hydrofoil (chord length c = 0.1 m), with x axis located on the chord line, y axis pointed upward, and z axis determined by the right-hand rule. The computational domain extends 10c upstream from the origin, 20c downstream, and ±10c in the y direction. The domain has a spanwise extension of 0.3c, which is no less than the typical computational spanwise length values (0.05c–0.1c [75-77], 0.2c [78, 79] and 0.3c [80]) in calculating the hydrofoil noise performance, ensuring

Just Accepted

accurate computational results with acceptable computational cost. The left, top and bottom boundaries are set as velocity inlet boundaries, the right boundary is defined as the pressure outlet boundary, and the two side walls in the spanwise z direction are defined as periodic boundaries, which are commonly used boundary conditions for hydrofoil noise simulation using FW–H acoustic analogy. The fluid is water with density of ρ = 998.2 kg/m^3, and dynamic viscosity of μ = 0.001003 Pa s. The hydrofoil surface is defined as the no-slip wall for the no-slip case, and it is defined as slip walls characterized by different slip lengths when the surface slip effects are considered. Note that the wall confinement effects of the domain on the hydrofoil acoustic characteristics are not considered in the present work. However, in practical experiments, acoustic measurements of the hydrofoil are usually carried out in the closed-loop cavitation tunnel, where the side wall confinement can impose a significant influence on the measured acoustic spectrum. Discussion on the effects of wall confinement on the hydrofoil acoustic characteristics can be found in the reference [81]. Due to the high computational cost for wall-resolved LES, which typically scales with $\mathrm{Re}^{13/7}$ [82], the chord-based Reynolds number in the present work is set in the moderate Reynolds number range of $\mathrm{Re} = \rho c U_0/\mu = 3.6\times10^5$ (freestream velocity U_0 = 3.618 m/s with zero angle of attack, which is extremely low Mach number flow considering the sound speed 1500 m/s in water) to ensure an acceptable computational cost and to validate with the experimental drag coefficient [83].

Six set of structured hexahedral meshes (M1–M6) are constructed for the whole computational domain, and the grid distribution can be seen in Fig. 3(b). Grid nodes are concentrated on the leading edge and trailing edge of the hydrofoil where the surface geometry curvature varies significantly. The cell numbers of the M1–M3 meshes are 6.95, 19.42, and 54.35 million, respectively, to ensure a fast flow convergence check, and the M4–M6 meshes are carefully refined based on the M3 mesh for final flow convergence check since the computational cost becomes

Just Accepted

significantly high beyond the M3 mesh. The cell numbers of the M4–M6 meshes are 64.56, 72.22, and 81.51 million, respectively. The height of the first cell layer y_0 is 6×10^{-6} m to ensure the $y^+ <1$ (y^+ is the wall-unit height distance, and in ANSYS Fluent y^+ is actually calculated based on the distance from the cell center to the wall d due to the finite volume method), and details of the M1–M6 meshes can be found in Table S2 in the ESM.

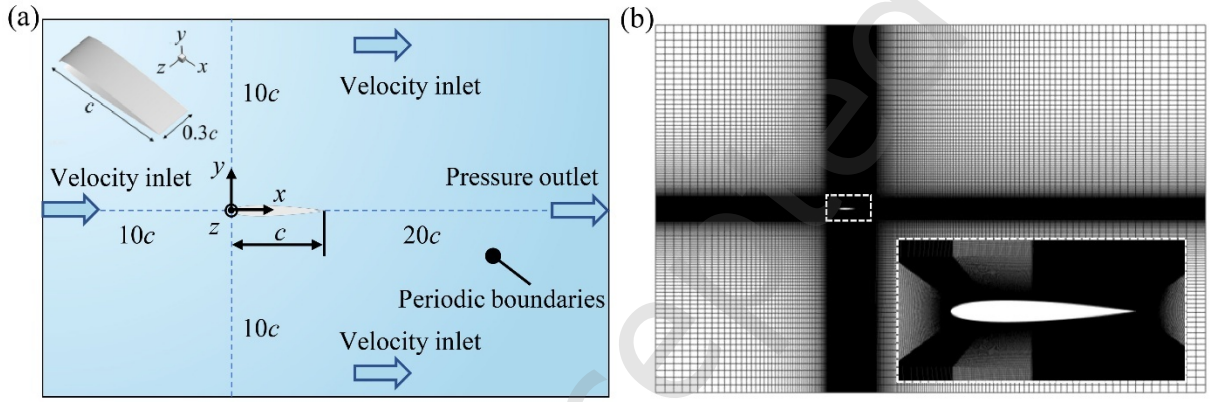


Figure 3 Numerical settings for the NACA 0012 hydrofoil simulation. (a) Computational domain and boundary conditions. (b) Mesh generation around the hydrofoil.

The present simulations are performed using the software ANSYS Fluent with the finite volume method. The pressure-based semi-implicit method for pressure-linked equations (SIMPLE) algorithm is employed to solve the governing equations. Compared with the coupled algorithm, the segregated SIMPLE algorithm can give faster overall solution time. Since the choice of the SIMPLE or the SIMPLE-Consistent (SIMPLEC) algorithm affects only the convergence rate of the flow, the more robust SIMPLE algorithm is employed for the current hydrofoil flow simulation. Convection terms are discretized using the bounded central differencing scheme due to the low numerical dissipation with maintained stability. Diffusion terms are discretized with the second order central differencing scheme. The transient terms are discretized using the bounded second order implicit scheme to achieve better stability as well as comparable accuracy to the second order implicit scheme. Gradients are calculated using the default least squares cell-based method due to

reduced computational cost than the node-based method, and the second order scheme is employed for pressure interpolation.

Flow convergence check is then performed on the M1–M6 meshes. A steady state SST k-ω simulation is firstly performed to ensure a faster convergence for the transient simulation. The time-step size for the large eddy simulation is chosen as $\Delta t = 2.0\times10^{-5}$ s ($\Delta t < \Delta x_{min}/U_0$, where Δx_{min} is the minimum streamwise grid size of the mesh), and 30000 time-steps corresponding to 21 flow-units (tU_0/c) of flow over the hydrofoil surface are carried out to ensure a statistically steady flow state. The instantaneous lift coefficient C_l [$C_l = F_l/(0.5\rho U_0^2 A)$, where F_l is the lift force, A is the platform area of the hydrofoil] and drag coefficient C_d [$C_d = F_d/(0.5\rho U_0^2 A)$, where F_d is the drag force] are analyzed. The time-averaged skin friction coefficient C_f [$C_f = \tau_w/(0.5\rho U_0^2)$, where τ_w is the total wall shear stress] and time-averaged pressure coefficient C_p [$C_p = (p-p_0)/(0.5\rho U_0^2)$, where p is the static pressure, p_0 is the ambient pressure] between time-steps of 20000–30000 are compared as well. Results are shown in Fig. 4. It can be found that with the increase of the cell number, the C_l, C_d, C_f, and C_p vary significantly for the M1–M4 meshes, and they gradually converge at the M5 and M6 meshes, since there are no significant differences in the force coefficients as well as the C_f and C_p profiles between the M5 and M6 meshes, especially in the flow transition position indicated by the abrupt increase in the C_f profiles. The pressure at the point of $x/c = 0.8$ at the midspan curve on the hydrofoil surface (Fig. S4 in the ESM) demonstrates similar convergence between the M5 and M6 meshes. The time-averaged drag coefficients of the M5 and M6 meshes in time-steps of 20000-30000 are around 0.0074, which is very close to the experimental value of 0.0079 [83]. The slightly higher value in the experiment can originate from the foil surface roughness and the tunnel wall effect. The y^+, $\Delta\xi^+$ and Δz^+ distributions of the M5 mesh are examined as well (Fig. S5 in the ESM), where $\Delta\xi^+$ is the wall-unit body-fit streamwise grid spacing, and Δz^+ is the wall-unit spanwise grid spacing. It is evident

Just Accepted

that the y^+ along the hydrofoil surface is below 1.0, the maximum value of $\Delta\xi^+$ is around 40 with most below 30, and most of the Δz^+ is below 30, which satisfy the requirements of the wall-resolved LES in that $y^+ < 1.0$, $\Delta\xi^+ \leq 50$, and $\Delta z^+ \leq 40$ [84]. Therefore, to save computational cost, the M5 mesh with 72.22 million cell numbers is adopted for further analysis and slip simulations.

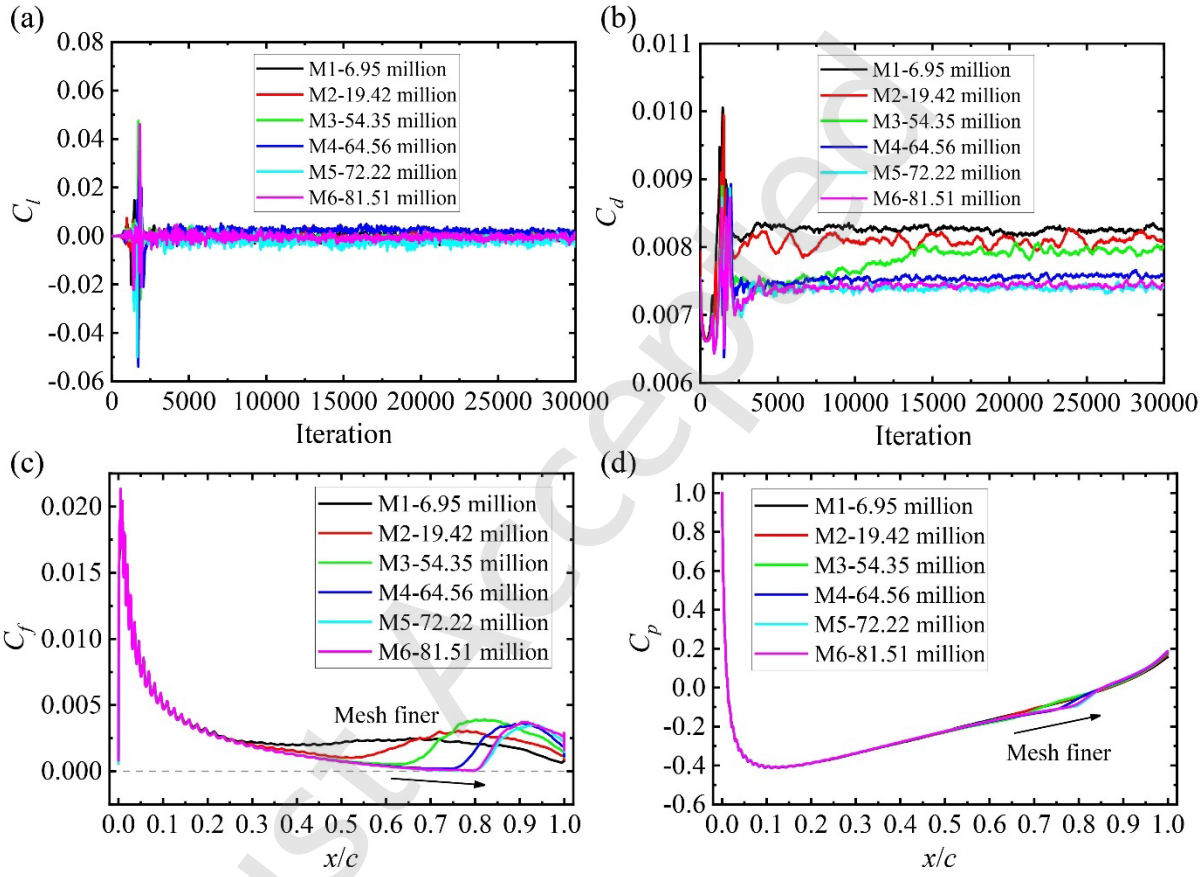


Figure 4 Grid convergence test for NACA 0012 hydrofoil. Lift coefficient variation (a) and drag coefficient variation (b) for the M1–M6 meshes. Time-averaged skin friction coefficient distribution (c) and pressure coefficient distribution (d) along the midspan curve on the hydrofoil surface for the M1–M6 meshes.

After the flow field calculation, the FW–H acoustic analogy is applied and another 10000 time-steps are performed on the M5 mesh for flow noise calculation and flow statistics sampling, which ensures a total 0.2 s flow statistics sampling and a 5 Hz frequency resolution in the sound pressure level spectrum. It has been discussed in Section 2.1 that for low Mach number flow (the

Mach number is extremely low with 0.0024 for hydrofoil in the present work), the dominant noise is the dipole loading noise and the impermeable surfaces are firstly recommended as the FW–H control surfaces to obtain high accuracy noise prediction. Therefore, the hydrofoil surface is selected as the FW–H control surface. For acoustic directivity evaluation, 36 acoustic receivers are circumferentially distributed along the circle with radius $r = 1000c$ centered at the hydrofoil trailing edge in the mid-span plane. The receiver located downstream of the hydrofoil trailing edge corresponds to the 0° direction, and the receiver located right above the hydrofoil trailing edge in the positive y direction corresponds to the 90° direction. The receivers are located sufficiently far with respect to the hydrofoil with $r = 1000c$ to record the far-field noise. For hydrofoils, the dominant frequency of the acoustic spectrum can range from several Hz to several thousand Hz [65]. For marine propellers, while the dominant frequency range is similar, the acoustic spectrum can be much more complex due to the ingested turbulence and hull wakes [66, 67, 85]. Particularly, the tonal and broadband characteristics of the marine propeller under nonuniform inflow can differ significantly from the uniform case [66]. For cases with cavitation, the acoustic spectrum evolution under different cavitation number also indicates complex noise generation mechanisms. Wang et al. [85] demonstrated that for a marine propeller operating in hull wakes, the tip vortex cavitation bursting is typically accompanied by significant broadband pressure fluctuations in the frequency range between the third and 13th blade passing frequency (BPF), and the occurrence of tip vortex cavitation bursting corresponds to increased wavelet energy within the third to 10th BPF range. As the cavitation number decreases, the dominant frequencies shift towards the low-frequency band. Based on the above considerations, the frequency range in the present work is selected as 25–3150 Hz to capture the most energetic part of the radiated noise of hydrofoils and propellers. The distance of $1000c$ ensures that only the far-field acoustic pressure fluctuations are being recorded based on the minimum interested frequency and the sound speed in water.

Just Accepted

The sound pressure level (SPL) of the NACA 0012 hydrofoil at the 90° receiver can therefore be obtained. It is known that the spanwise length can influence the spanwise coherence of the acoustic sources and the resulting noise levels. In the present simulations, the reported sound pressure levels correspond to the simulated span of (0.3c) and no spanwise length correction has been applied. As shown in Fig. 5, several discrete tonal peaks are superimposed on the broadband spectrum, with representative dominant tones indicated by arrows. These dominant tones are accompanied by several smaller peaks, consistent with the acoustic features reported for laminar-flow airfoils [86]. The power spectral density of surface pressure fluctuations (denoted by S_{pp}) is calculated from the leading edge to the trailing edge of the hydrofoil along the midspan curve by using the Welch method and Hanning window. A comparison between SPL and S_{pp} reveals that the discrete tones in the SPL correlate well with those in the S_{pp} with identical frequencies upstream of $x/c = 0.5$, whereas such tones are absent in the S_{pp} downstream of $x/c = 0.6$. Given that the flow field around the NACA 0012 hydrofoil (Fig. S6 in the ESM) exhibits discrete separation bubbles beyond $x/c = 0.7$ and that transition to turbulence occurs at $x/c = 0.8$, while the tonal peaks correlate with the pressure fluctuations only within the laminar boundary layer region (upstream of $x/c = 0.5$), this indicates that the discrete tonal noise in the far field therefore originates from the laminar boundary layer instability rather than from the separated flow or turbulent structures [60, 86].

Just Accepted

This is a Just Accepted version, keep updated with https://doi.org/10.26599/OCEAN.2026.9470035

OCEAN 2026, 2, 9470035

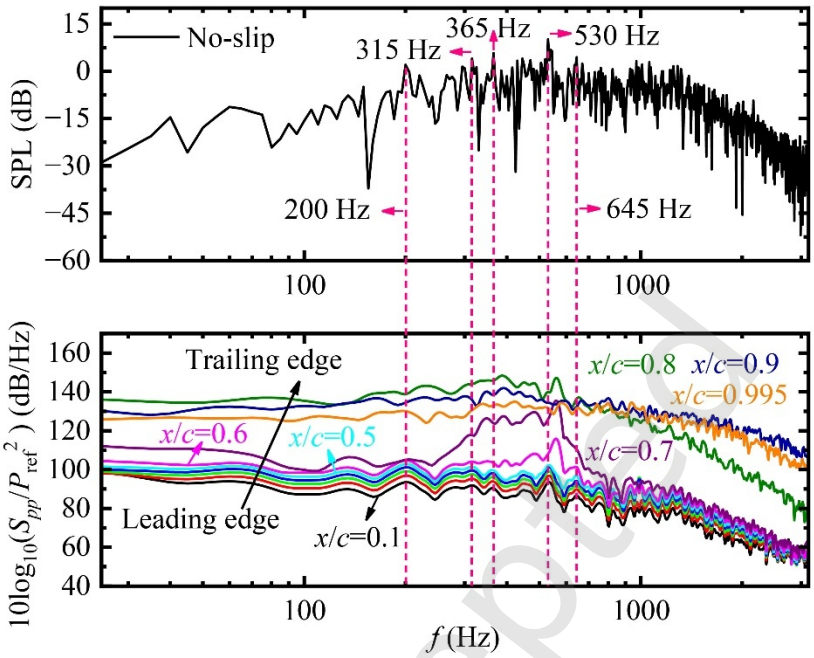


Figure 5 Sound pressure level spectrum at the 90° receiver and power spectral density of pressure fluctuations along the hydrofoil surface for the no-slip case.

2.3 Slip boundary condition implementation and validation

The Navier slip model is adopted in the present study to represent the practical superhydrophobic surfaces due to the model simplicity and high accuracy. The implementation of the slip boundary to the hydrofoil surface is illustrated in Fig. 6. For a given slip length L_s, the slip velocity at the solid-liquid interface can be expressed as $U_s = L_s(\partial u/\partial y) = L_s(U_c - U_s)/d$, where U_c is the cell velocity of the first layer near the surface, and d is the distance between the first layer cell center and the surface. The slip boundary can be implemented through the user-defined function (UDF) in ANSYS Fluent, which allows different slip lengths to be prescribed and applied to the solid surfaces of interest. Once the slip boundary code is implanted, the slip velocity can be obtained by solving the Navier–Stokes equations coupled with the slip boundary condition.

It should be noted that in the discrete slip relation $U_s = L_s(\partial u/\partial y) = L_s(U_c - U_s)/d$, the wall velocity gradient is approximated by a first-order difference, and the accuracy of this

Just Accepted

This is a Just Accepted version, keep updated with https://doi.org/10.26599/OCEAN.2026.9470035

OCEAN 2026, 2, 9470035

approximation is first order in d. The implementation has been validated by the previous work (Figs. S7 and S8 in the ESM [48]). Together with the fact that the present mesh resolves the near-wall region sufficiently ($y^+ < 1$)) and the values of the defined ratio $\lambda = L_s / y_0$ (y_0 is the first cell layer height and $y_0 = 2d$ for the present hexahedral boundary layer mesh) fall within the range employed in previous studies (Table S3 in the ESM), the accuracy of the slip implementation is not expected to deteriorate as L_s increases from 10 to 500 μm under the present simulations.

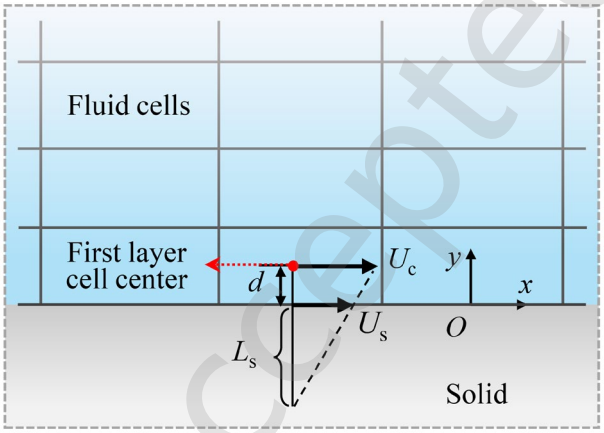


Figure 6 Illustration of surface slip implementation.

According to Table S1 in the ESM, slip lengths obtained on superhydrophobic surfaces can reach hundreds of micrometers. Previous studies [44, 46-48, 87-89] have investigated a wide range of slip lengths from several micrometers to hundreds of micrometers, therefore it is necessary to investigate a wide range of slip lengths on the hydrofoil noise performance to fully understand the slip effects and underlying mechanisms. Based on this consideration, nine slip lengths covering small slip lengths (10 μm, 20 μm), moderate slip lengths (50 μm, 100 μm, 180 μm), relatively large slip lengths (210 μm, 230 μm), and large slip lengths (250 μm, 500 μm) are determined to ensure a systematic investigation. Slip boundary conditions are applied in both the streamwise and spanwise directions to better model the three-dimensional effects, and both the upper and lower surfaces of the hydrofoil are treated as slip walls.

Just Accepted

Despite the simplicity in adopting the Navier slip length model, it needs to be noted that there still exist some assumptions and limitations in using this model. As demonstrated in the Introduction, previous results [38, 39] have shown that for texture sizes as large as $L^+ \leq 25$ (L^+ is the texture pattern spacing in wall unit), the superhydrophobic surfaces with heterogeneous textures can be well modeled with the homogeneous Navier slip boundary. In the present work, it is estimated that the texture pattern spacing has to be limited to about one hundred micrometer to satisfy $L^+ \leq 25$. Also, the idealized Navier slip model assumes that the slip length remains constant along the hydrofoil surface without being influenced by external flow conditions and therefore prohibits the disappearance of slip effects in simulations. However, in practical applications, the gas layer on the superhydrophobic surfaces may be depleted under harsh environment leading to the disappearance of the slip effects. Therefore, although the Navier slip length model can accurately represent realistic superhydrophobic surfaces in most cases, discrepancies between this idealized model and practical surfaces under harsh environments should be treated with caution.

3 Results and discussion

This section presents detailed hydrodynamic and flow noise results of the hydrofoil under different surface slip lengths. The flow field around the hydrofoil are comprehensively analyzed to unravel the underlying mechanisms of flow noise variation.

3.1 Effects of surface slip on hydrodynamics

For hydrodynamic performances, the lift coefficient C_l and drag coefficient C_d are analyzed. The instantaneous lift coefficient C_l and drag coefficient C_d are decomposed into the time-averaged components ($\overline{C}_l$, $\overline{C}_d$) and the fluctuating components (C_l', C_d'). Here, we define the rms lift coefficient reduction rate $\Delta C_l'_{\text{rms}}$ and the time-averaged drag reduction rate $\Delta\overline{C}_d$ as

$$\Delta C_l'_{\text{rms}}\,(\%) = \frac{C_l'_{\text{rms-noslip}} - C_l'_{\text{rms-slip}}}{C_l'_{\text{rms-noslip}}} \times 100\% \tag{11}$$

Just Accepted

$$\Delta\overline{C}_d\,(\%) = \frac{\overline{C}_{d\text{-noslip}} - \overline{C}_{d\text{-slip}}}{\overline{C}_{d\text{-noslip}}} \times 100\% \tag{12}$$

in which the quantities with subscript "noslip" and "slip" denote the values in no-slip and slip cases, respectively.

The instantaneous lift and drag coefficients under different slip lengths can be seen in Fig. 7, and the rms of lift coefficient fluctuations and the time-averaged drag coefficient under different slip lengths can be further seen from Fig. S9 in the ESM. As shown in Figs. 7a–c, both the lift and drag coefficients demonstrate significant fluctuations over time. For the lift coefficient, the time-averaged value is approximately zero due to the geometrical symmetry and zero angle of attack, while the fluctuations of the lift coefficient vary significantly under different slip lengths. With the increase of the slip length, the lift coefficient fluctuations demonstrate a non-monotonic trend, characterized by an initial decrease, an increase, a second decrease, and a final increase. Fourier spectra of the instantaneous lift coefficient in Fig. 7d show that there clearly exist several characteristic frequencies for the no-slip, 10 μm, 20 μm, 50 μm, 100 μm, 180 μm, 250 μm, and 500 μm slip cases. The dominant frequencies in the Fourier spectrum of the no-slip case correspond well to those in the SPL spectrum shown in Fig. 5.

Just Accepted

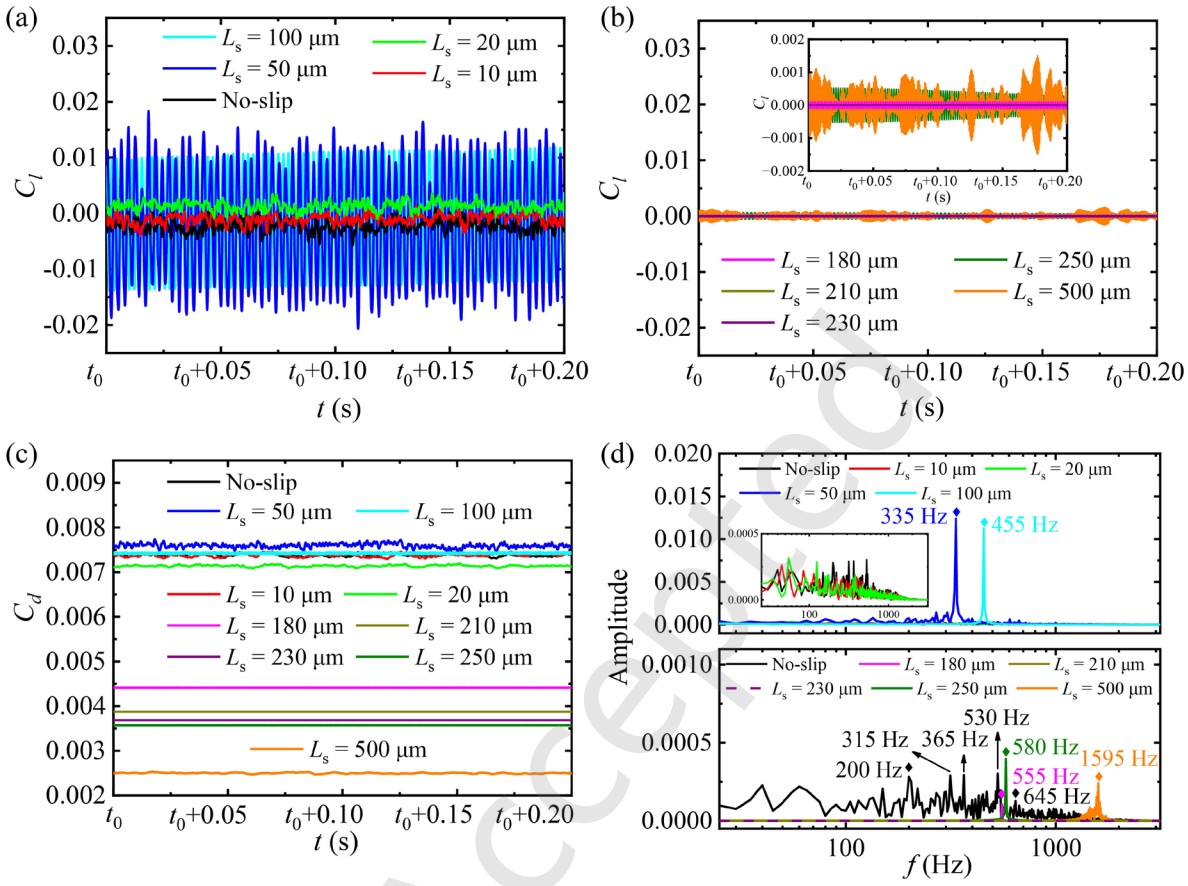


Figure 7 Variation of lift coefficient and drag coefficient of the NACA 0012 hydrofoil under different slip lengths. Lift coefficient for the no-slip case and L_s = 10, 20, 50, 100 μm slip cases (a) and L_s = 180, 210, 230, 250, 500 μm slip cases (b). (c) Drag coefficient. (d) Fourier spectra of the lift coefficient.

For the drag coefficient, it demonstrates a non-monotonic variation as well. It can be found in Fig. S9 in the ESM that for small slip lengths of 10 μm and 20 μm, drag coefficient is slightly reduced compared to the no-slip case. While for moderate slip lengths of 50 μm and 100 μm, the drag coefficient is slightly increased. Further increasing the slip length leads to significantly increased drag reduction rate from 40.3% to 66.2% with slip length increasing from 180 μm to 500 μm. The non-monotonic variation of the drag coefficient is quite interesting, and the flow field is therefore further examined.

The instantaneous velocity magnitude and wall shear stress on the hydrofoil surface are firstly

Just Accepted

examined, as shown in Figs. S10 and S11 in the ESM. It can be found that with the increase of the slip length, the slip velocity gradually increases, the distributed area for larger slip velocity also expands, and the wall shear stress shows a general decrease with increasing slip length. The time-averaged skin friction coefficient and the streamwise velocity distribution at the midspan curve along the hydrofoil surface are then extracted. It can be found in Fig. 8 that with the increase of the slip length, the skin friction coefficient decreases, and the streamwise surface velocity increases, which are in accordance with the results in Figs. S10 and S11. Together with the local velocity flow field around the hydrofoil in Fig. S12 in the ESM, it can be found that for the 10 μm and 20 μm slip cases, flow transition is not significantly postponed downstream, and the separation bubbles in the rear part of the hydrofoil are only slightly weakened compared to the no-slip case (Fig. S6 in the ESM). This is possibly due to that the slip length values are relatively small and that there is a competition between the streamwise and the spanwise slip. Since streamwise slip delays flow transition and reduces the frictional drag, while spanwise slip often induces strengthened streamwise vortex, prohibits flow transition delay, and then increases the frictional drag [90], the overall effect is that flow transition is not significantly delayed due to the relatively small streamwise slip length values, and the overall drag coefficient is only slightly reduced.

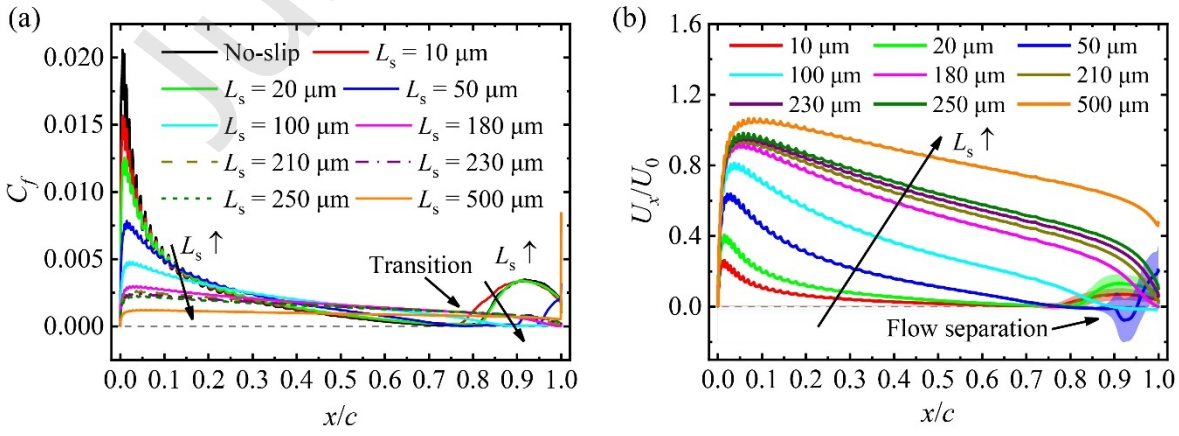


Figure 8 Time-averaged skin friction coefficient (a) and streamwise velocity distribution (b) along the

midspan curve on the hydrofoil surface under different slip lengths. The colored shadows around the solid lines indicate the velocity fluctuations.

For the moderate 50 μm slip case, it can be found from Fig. 8 that the skin friction coefficient near the hydrofoil trailing edge firstly reaches zero, then increases, and then decreases to zero again along the streamwise direction on the hydrofoil surface, and there exists a closed backflow region demonstrated in the streamwise velocity profile in the range of x/c = 0.90–0.95, which indicates the existence of large laminar separation bubbles. For the 100 μm slip case, the skin friction coefficient in the vicinity of the trailing edge vanishes to zero since x/c = 0.9, indicating the existence of large non-attached flow separation area near the hydrofoil trailing edge. This has also been clearly demonstrated in Fig. S12 in the ESM. For the 50 μm and 100 μm slip cases, the total drag increase may be induced by the competition between the pressure drag increase and frictional drag decrease [48], since flow separation can significantly alter the pressure coefficient distribution and increase the pressure drag compared to the attached flow (as shown in Fig. S13 in the ESM). The flow shows a very weak separation at the hydrofoil trailing edge for the 180 μm slip case, and becomes fully attached and back to laminar state for the 210–500 μm slip cases. Therefore, the total drag is significantly reduced.

The above results demonstrate that surface slip can have significant effects on the hydrofoil hydrodynamic performance in generally delaying flow transition, forcing the flow back to laminar state, and reducing the total drag, which are consistent with previous studies [48, 90-92]. However, surface slip can also induce slight drag increase due to pressure drag increase caused by large flow separation or separation bubbles near the hydrofoil trailing edge. In addition, surface slip has also demonstrated significant effects on the instantaneous lift coefficient and flow unsteadiness, which suggests the potential influence on the flow noise performance.

3.2 Effects of surface slip on flow noise characteristics

Just Accepted

The noise performance of the hydrofoil at the 90° receiver can be seen in Fig. 9. It can be found that compared to the no-slip case, the sound pressure level spectra of the 10 μm and 20 μm slip cases demonstrate similar discrete tonal peaks among the broadband profile with however decreased values. For the 50 μm, 100 μm and 180 μm slip cases, significant tonal peaks begin to appear with the dominant frequency located at f = 335 Hz, f = 455 Hz, and f = 555 Hz, respectively. Further increasing the slip length leads to significantly reduced broadband noise for the 210 μm, and 230 μm slip cases, and the noise is extremely low considering the laminar flow state. However, counterintuitive phenomena begin to occur for the 250 μm and 500 μm slip cases, as there appear significant high tonal peaks again. All the tonal peaks correspond well with the characteristic peaks in the Fourier spectra of the lift coefficient. However, for the 500 μm case, slight discrepancy exists between the 1595 Hz in the lift coefficient (Figure 7) and 1586 Hz in the sound pressure level spectrum (Figure 9). By closely examining the spectra, it can be found that the tone near 1.6 kHz for the 500 μm slip case is not an isolated narrow line but a cluster of sub-peaks of comparable amplitude on a broadband hump. For such a tone cluster, the location of the "dominant peak" is actually hard to recognize and sensitive to the broadband fluctuations. This might be due to that the two-dimensional vortex shedding undergoes three-dimensional breakdown at 500 μm slip case (seen from Fig. 11 in Section 3.3), and that the spanwise coherence of the shedding gradually loses. By contrast, for the 250 μm slip case, where the shedding remains two-dimensional (seen from Fig. 11 in Section 3.3), the tone is an isolated narrow line significantly above the broadband floor, and the peak frequencies read from the lift and far-field spectra coincide exactly. Despite that, the discrepancy between the two peak frequencies for the 500 μm slip case is only about 0.6% (~9 Hz), which can be stated that the tones appear at about 1.59 kHz.

Based on the results in Fig. 9, the OASPL of the hydrofoil under different slip lengths at the 90° receiver in the far field can be calculated using Equation (10) and converted to the OASPL at

Just Accepted

the standard distance of 1 m by $\mathrm{OASPL}|_{1\ \mathrm{m}} = \mathrm{OASPL}|_r + 20\log_{10}(r)$ for comparison [72]. Differences of the flow noise between the slip cases and the no-slip case can be found in Fig. S14 in the ESM. It can be found that the OASPL is decreased for the 10 μm and 20 μm slip cases, while increased for the 50 μm and 100 μm slip cases, and then significantly decreased for the 180–230 μm cases. However, the OASPL begins to increase again for the 250 μm and 500 μm slip cases. Therefore, the OASPL of the hydrofoil demonstrates a non-monotonic variation with a first decrease, a followed increase, a second decrease, and a final increase.

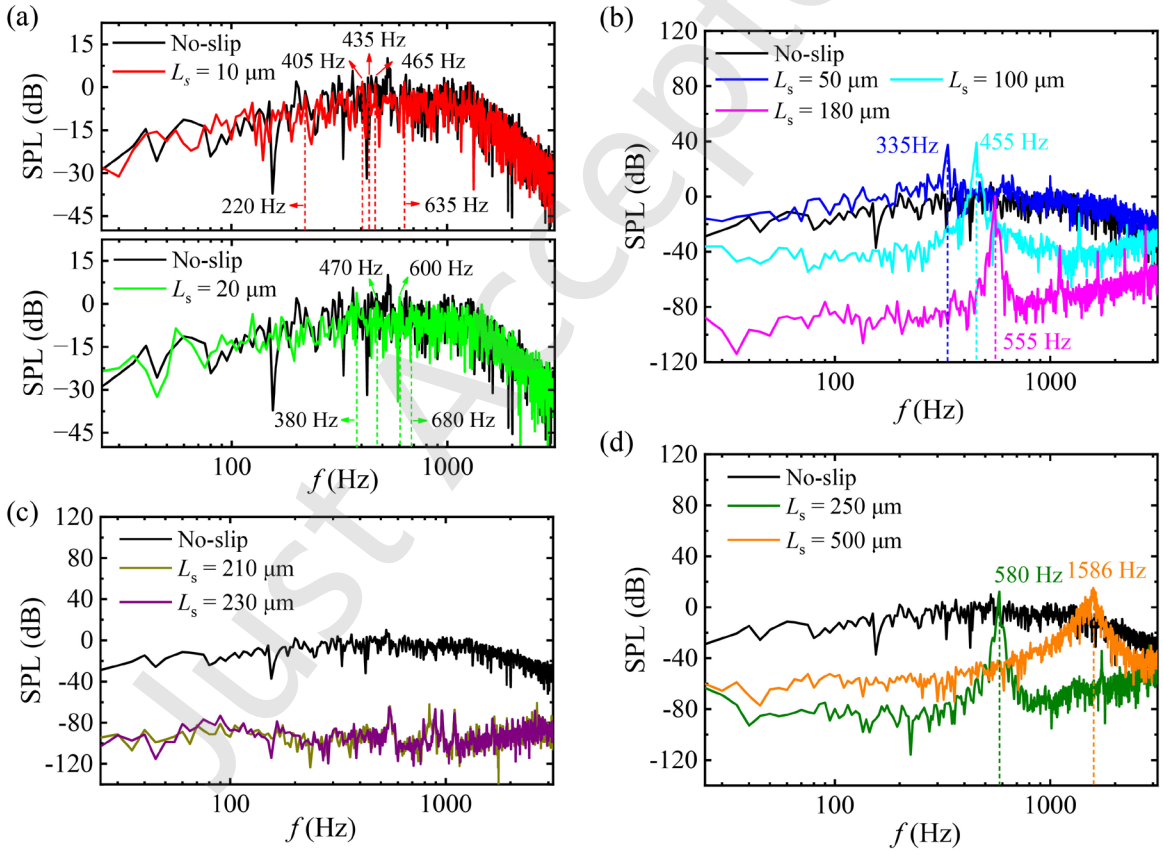


Figure 9 Sound pressure level of the NACA 0012 hydrofoil under different slip lengths compared to the no-slip case. (a) L_s = 10, 20 μm. (b) L_s = 50, 100, 180 μm. (c) L_s = 210, 230 μm. (d) L_s = 250, 500 μm.

The directivity of the OASPL in the midspan plane of the hydrofoil has also been examined. It can be found from Fig. 10 that the OASPL presents an “8” like acoustic directivity, which is in

accordance with the radiation characteristics of the dipole noise. This "8" like acoustic directivity remains unchanged for the slip cases, which indicates that surface slip does not change the sound radiation characteristics of the hydrofoil. Also, the variation of the OASPL under different slip lengths resembles that of the 90° angle with increasing slip length.

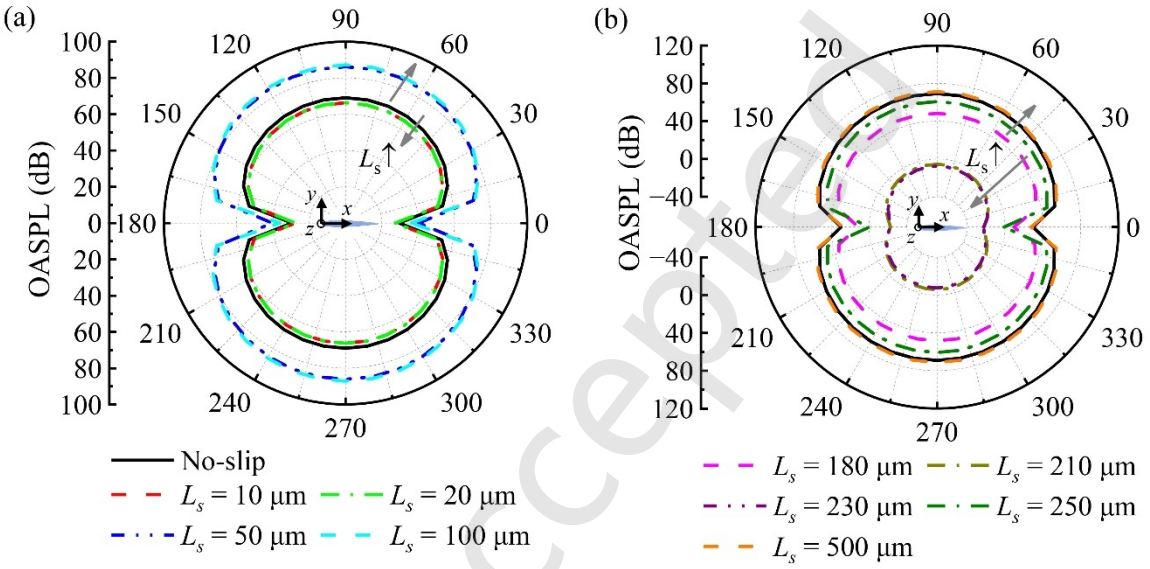


Figure 10 Overall sound pressure level directivity at 360° circumferential angles in the midspan plane under different slip lengths compared to the no-slip case. (a) L_s = 10, 20, 50, 100 μm. (b) L_s = 180, 210, 230, 250, 500 μm.

The non-monotonic variation of the OASPL is interesting, and has not been discovered before. In the following sections, detailed flow field and power spectra density of surface pressure fluctuations will be examined to unravel the underlying mechanisms.

3.3 Overall flow field around the hydrofoil surface

To elucidate the mechanisms for flow noise variation under surface slip, overall flow field around the hydrofoil surface are firstly examined. Flow structures characterized by the Q criterion are examined, where $Q = 0.5\ (\|\Omega\|_F^2 - \|S\|_F^2)$, $\Omega = 0.5\ (\partial u_i/\partial x_j - \partial u_j/\partial x_i)$, $S = 0.5\ (\partial u_i/\partial x_j + \partial u_j/\partial x_i)$, and $\|\ \|_F$ denotes the Frobenius norm. It can be found from Fig. 11 that for the no-slip case, flow

structures near the hydrofoil leading edge are evenly distributed in the spanwise direction, and three-dimensional turbulent structures appear in the rear part of the hydrofoil. For slip cases, the flow structures around the hydrofoil are significantly changed. For the 10 μm and 20 μm slip cases, the regions for the laminar flow structures are slightly enlarged. For the 50 μm and 100 μm slip cases, the flow structures near the hydrofoil trailing edge demonstrate two-dimensional wake characteristics in the spanwise direction, indicating the existence of periodic vortex shedding. For the 180 μm slip case, the hydrofoil surface is nearly in full laminar flow state, with enhanced two-dimensionality in the wake structures. For the 210 μm and 230 μm slip cases, the hydrofoil surface is in full laminar state, and the laminar flow structures in the hydrofoil wake are also significantly suppressed. However, wake unsteadiness for the 250 μm case is enhanced again, and strong three-dimensional turbulent structures appear for the 500 μm slip case.

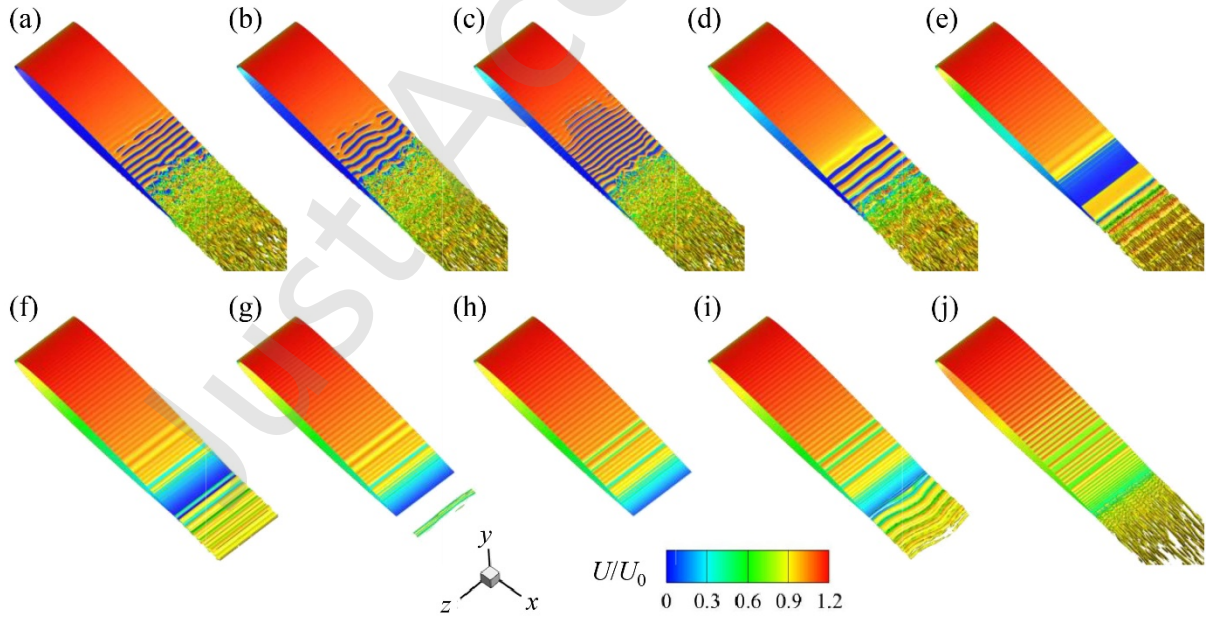


Figure 11 Iso-surfaces of $Qc^2/U_0^2 = 8$ colored by velocity magnitude under different slip lengths. (a) No-slip case. (b) 10 μm slip. (c) 20 μm slip. (d) 50 μm slip. (e) 100 μm slip. (f) 180 μm slip. (g) 210 μm slip. (h) 230 μm slip. (i) 250 μm slip. (j) 500 μm slip.

JustAccepted

This is a Just Accepted version, keep updated with https://doi.org/10.26599/OCEAN.2026.9470035

OCEAN 2026, 2, 9470035

The above results reveal that surface slip can impose complex effects on flow structures around the hydrofoil surface. Effects of surface slip on surface pressure fluctuations are examined, as shown in Fig. 12. It can be found that for the no-slip case, surface pressure fluctuations first increase and then decrease along the streamwise direction from the hydrofoil leading edge to trailing edge. Therefore, there exists a maximum fluctuating region in the rear part of the hydrofoil surface. For 10 μm and 20 μm slip cases, surface pressure fluctuations are significantly decreased. While for 50 μm and 100 μm slip cases, the maximum fluctuation region gradually moves downstream to the trailing edge of the hydrofoil. For 180–230 μm slip cases, surface pressure fluctuations are at extremely low levels due to the laminar flow on the hydrofoil surface. However, for large slip lengths of 250 μm and 500 μm, surface pressure fluctuations near the trailing edge of the hydrofoil begin to increase again.

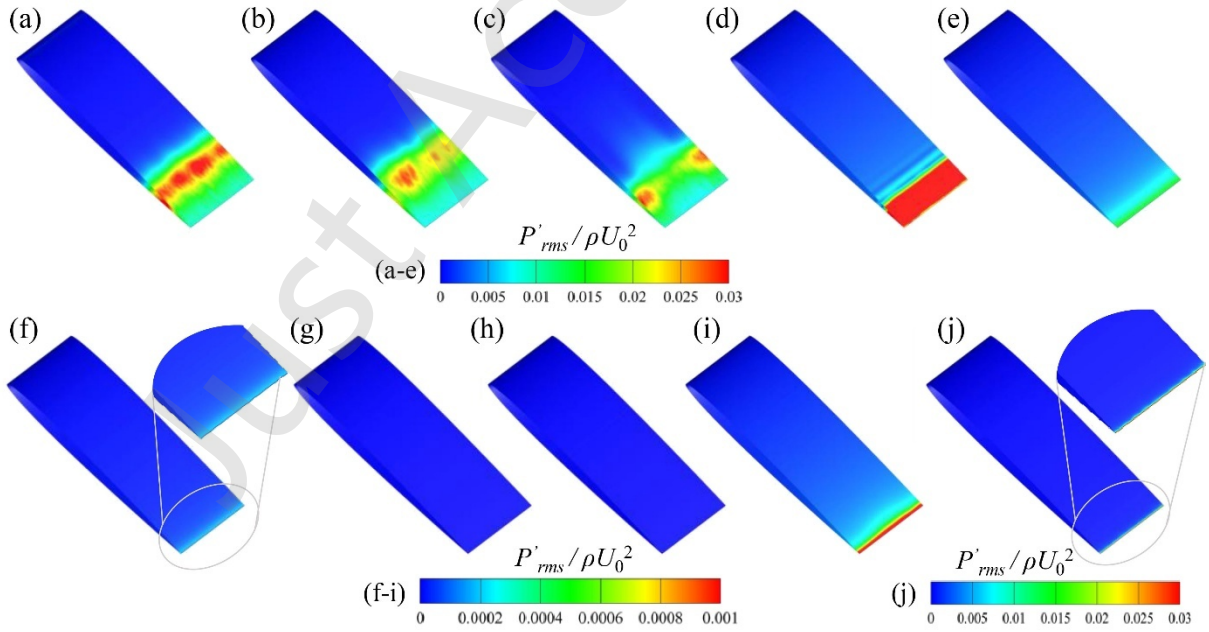


Figure 12 Distribution of root mean square of surface pressure fluctuations under different slip lengths. (a) No-slip case. (b) 10 μm slip. (c) 20 μm slip. (d) 50 μm slip. (e) 100 μm slip. (f) 180 μm slip. (g) 210 μm slip. (h) 230 μm slip. (i) 250 μm slip. (j) 500 μm slip.

Just Accepted

Furthermore, the distribution of the surface pressure fluctuations along the midspan curve on the hydrofoil surface are shown in Fig. S15 in the ESM. It can be found that the location of the maximum surface pressure fluctuations coincides with the flow transition point on the hydrofoil surface for slip lengths below 50 μm. For slip cases with non-attached flow separation or wake unsteadiness (100 μm, 180 μm, 250 μm, and 500 μm), surface pressure fluctuations gradually increase along the hydrofoil surface from leading edge to trailing edge. For slip cases with purely laminar flow on the hydrofoil surface (210 μm and 230 μm), surface pressure fluctuations keep sufficiently low. It can be seen that the pressure fluctuations at the hydrofoil trailing edge also exhibit a decrease–increase–decrease–increase variation with increasing slip length, which resembles that of the OASPL.

The distribution of the turbulent kinetic energy (TKE) near the hydrofoil trailing edge is examined as well. TKE is the kinetic energy of the turbulent fluctuation motions in the flow field, and the distribution of TKE can reflect both the magnitude and the area of turbulent fluctuations. As shown in Fig. 13 and Fig. S16 in the ESM, flow regions with high TKE are gradually pushed downstream along the hydrofoil surface and then into the hydrofoil wake with increasing slip length below 180 μm. TKE becomes increasingly high for the 50 μm and 100 μm slip cases and extremely low for the 210 μm and 230 μm slip cases. However, it increases again for large slip lengths of 250 μm and 500 μm, with high TKE appeared in the hydrofoil wake and at the hydrofoil trailing edge, respectively.

Just Accepted

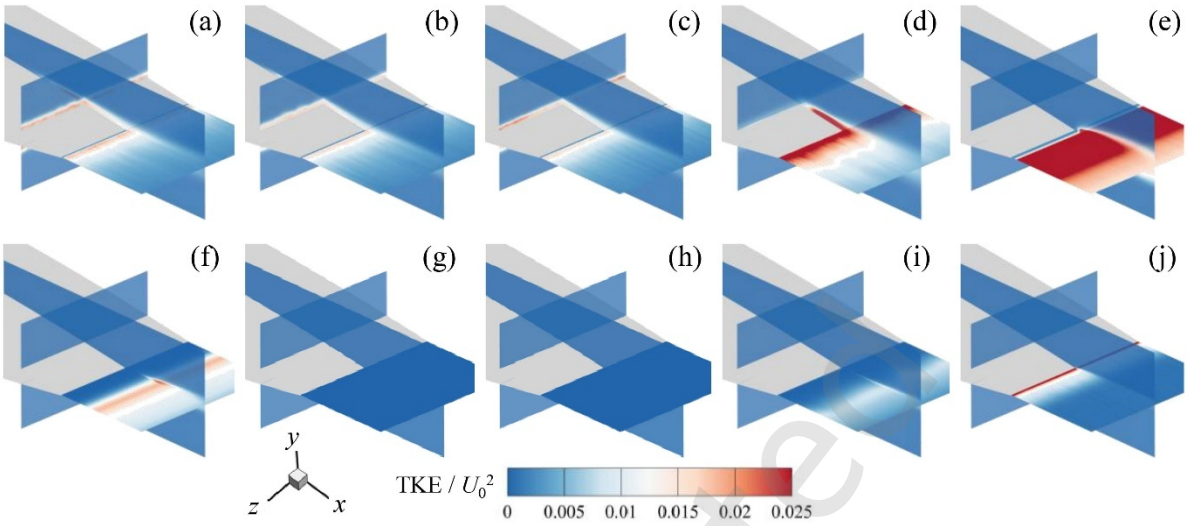


Figure 13 Turbulent kinetic energy distribution around the hydrofoil trailing edge. (a) No-slip case. (b) 10 μm slip. (c) 20 μm slip. (d) 50 μm slip. (e) 100 μm slip. (f) 180 μm slip. (g) 210 μm slip. (h) 230 μm slip. (i) 250 μm slip. (j) 500 μm slip.

Power spectrum analysis of pressure fluctuations are further investigated. A series of points are monitored along the midspan curve of the hydrofoil surface in the streamwise direction from leading edge to trailing edge (x/c = 0.1–0.995). The power spectral density of pressure fluctuations (S_{pp}) for the no-slip and slip cases are shown in Fig. 14. For the 10 μm and 20 μm slip cases, SPL spectra at the 90° receiver are compared with S_{pp} as well (Fig. S17 in the ESM). Similar to that of the no-slip case, the discrete tones appeared in the SPL spectra corelate well with those in S_{pp} in the front part of the hydrofoil with same frequencies for the 10 μm and 20 μm slip cases, indicating that the same tonal noise generation mechanism due to laminar boundary layer instability persists at these slip lengths. Since surface slip can stabilize the attached boundary layer [87], the instability of the boundary layer is likely attenuated and the flow separation bubbles are slightly weakened (Fig. S12 in the ESM), which may account for the weakened tonal peaks in the 10 μm and 20 μm slip cases. For slip lengths of 50–180 μm, the S_{pp} becomes quite different, demonstrating pronounced tonal peaks from the hydrofoil leading edge to the trailing edge. This can be attributed

Just Accepted

to the strong separation bubbles and separated shear layers induced by surface slip, which locks the vortex shedding in a narrow frequency band and thereby sharpens the tonal peaks. The above behavior of the 50–180 μm slip cases resembles the acoustic feedback loop proposed for airfoil tonal noise in compressible flows [56, 93], where the loop acts as a frequency selection mechanism and subsequently imparts greater regularity to the pre-existing vortex shedding. However, since the present approach combines the incompressible LES with one-way FW–H acoustic analogy and does not explicitly resolve the upstream propagating acoustic waves or their feedback on the boundary layer, the existence of such an acoustic feedback loop cannot be resolved or verified within the present numerical framework. Further increasing the slip length, significantly different variation has occurred. For the 210 μm and 230 μm slip cases, the S_{pp} is in extremely low level, and shows no significant difference along the streamwise direction. While for the 250 μm and 500 μm slip cases, the S_{pp} demonstrates significant tonal peaks again along the entire hydrofoil surface.

Just Accepted

This is a Just Accepted version, keep updated with https://doi.org/10.26599/OCEAN.2026.9470035

OCEAN 2026, 2, 9470035

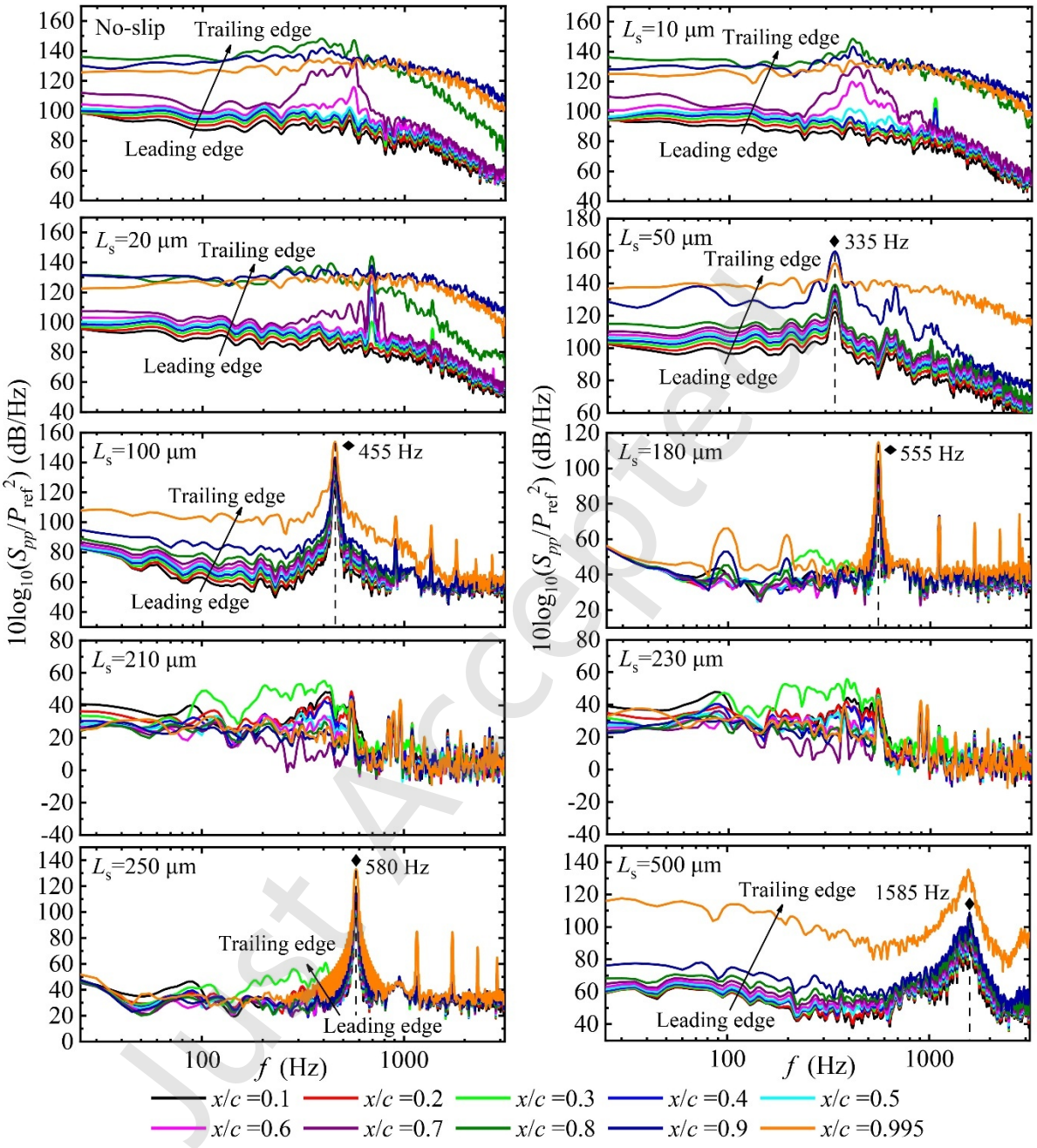


Figure 14 Power spectral density of surface pressure fluctuations along the midspan curve on the hydrofoil surface under different slip lengths.

It can be known from the above results that, for the no-slip case and 10 μm and 20 μm slip cases, the laminar boundary layer instability mechanism dominates the flow noise generation especially for the discrete tonal peaks. Surface slip can help to reduce the tonal peaks, and therefore

decrease the OASPL. As slip length increases, more pronounced tonal peaks appear in the cases of 50–180 μm. This can be attributed to the strong separation bubbles and separated shear layers induced by surface slip, which concentrates the shedding energy in a narrow frequency band. The OASPL is therefore increased for the 50 μm and 100 μm slip cases, while decreased for the 180 μm slip case due to the significantly reduced broadband noise. Since the flow on the hydrofoil surface of the 210 μm and 230 μm slip cases is fully laminar, the OASPL is the lowest due to the extremely low broadband noise. However, significantly high tonal peaks appear again for the 250 μm and 500 μm slip cases, leading to the increase of OASPL in the 500 μm slip case. Since the OASPL behavior is strongly influenced by the tonal peaks, especially the pronounced peaks appeared in the 50 μm, 100 μm, 180 μm, 250 μm and 500 μm slip cases, the origins of those peaks need to be checked.

3.4 Local flow field around the hydrofoil trailing edge

The above results have shown that the OASPL is strongly influenced by the pronounced tonal peaks in the 50 μm, 100 μm, 180 μm,250 μm and 500 μm slip cases. Therefore, this section aims to examine the local flow field near the hydrofoil trailing edge to gain better understanding of the origins of those peaks.

The distribution of the instantaneous spanwise vorticity in the midspan plane of the hydrofoil is examined to understand the flow field evolution near the hydrofoil trailing edge, as shown in Fig. 15. For the no-slip case, there exist counterrotating random turbulent vortex structures at the upper and lower surfaces of the hydrofoil. With increasing slip length, the turbulent vortex structures are pushed downstream toward the trailing edge. For the 50 μm and 100 μm slip cases, discontinuous vortex shedding structures can be apparently seen in the range of x/c = 0.90–1.00 and x/c = 0.95–1.10, respectively. For the 180 μm slip case, vortex shedding in the range of x/c = 1.05–1.15 can be clearly seen. For the 210 μm slip case, steady laminar flow structures are found

Just Accepted

near the hydrofoil surface and in the hydrofoil wake. However, wake instability appears in the range of x/c = 1.05–1.15 for the 250 μm slip case and random turbulent vortex structures emerge in the range of x/c = 1.00–1.05 for the 500 μm slip case.

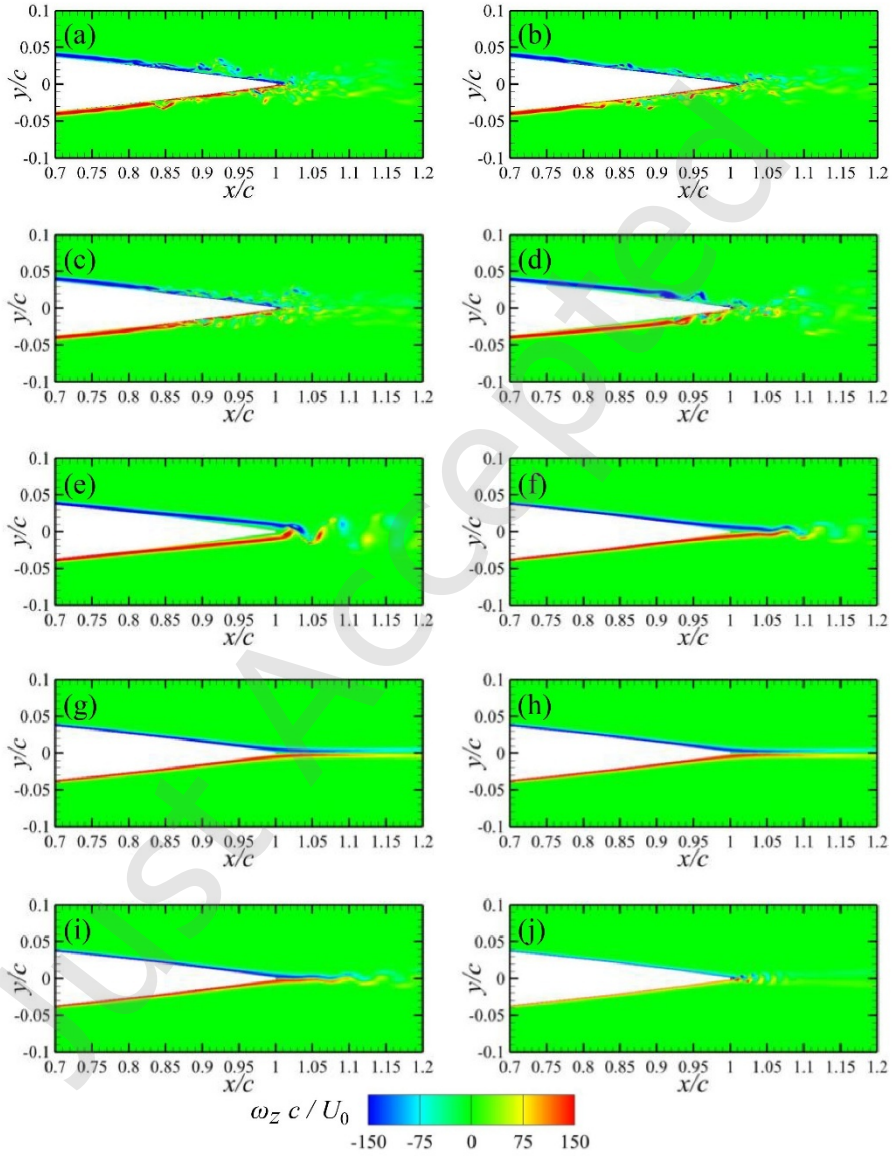


Figure 15 Instantaneous spanwise vorticity distribution around the hydrofoil trailing edge. (a) No-slip case. (b) 10 μm slip. (c) 20 μm slip. (d) 50 μm slip. (e) 100 μm slip. (f) 180 μm slip. (g) 210 μm slip. (h) 230 μm slip. (i) 250 μm slip. (j) 500 μm slip.

The above results demonstrate that there appears discontinuous vortex shedding for the 50 μm,

100 μm and 180 μm slip cases where tonal noise significantly increases. It can be further known from Fig. S12 in the ESM and Fig. 15 that there is either flow separation bubble or non-attached flow separation near the hydrofoil trailing edge for the 50 μm, 100 μm, and 180 μm slip cases. Therefore, it can be deduced that the pronounced tonal peaks for the 50 μm, 100 μm, and 180 μm cases mainly originate from the periodic vortex shedding due to flow separation on the hydrofoil surface. For the 250 μm and 500 μm slip cases, strong tonal noise increases again despite that the hydrofoil surface is in laminar flow. This suggests that there must exist a different tonal noise generation mechanism for the 250 μm and 500 μm slip cases from that of the 50 μm, 100 μm, and 180 μm cases. Previous works [48, 94, 95] have demonstrated that surface slip can decrease the displacement thickness of the boundary layer, and the truncated hydrofoil trailing edge has been found to induce periodic vortex shedding due to bluntness [96]. Therefore, it is inferred that for the 250 μm and 500 μm slip cases the tonal peaks originate from the vortex shedding due to the enhanced bluntness effect of the hydrofoil trailing edge induced by large slip lengths.

To verify the bluntness effect of the hydrofoil, the nondimensional boundary layer displacement thickness at the trailing edge (δ^*/c) is extracted and plotted against the slip length, as shown in Fig. S18 in the ESM. The relative ratio of the trailing edge geometric thickness (h = 0.25 mm) of the NACA 0012 hydrofoil to the boundary layer displacement thickness (δ^*) is also plotted. It can be seen that δ^*/c gradually decreases with the increase of the slip length in the range of 210–500 μm, while h/δ^* gradually increases and reaches 0.2 for the 500 μm slip length. Therefore, the bluntness effect of the hydrofoil trailing edge gradually enhances with increasing slip length.

Since the flow regimes of a typical blunt body such as the circular cylinder is usually characterized by the Reynolds number (Re) based on the cylinder diameter and the incoming flow velocity, therefore we define a characteristic Reynolds number Re_{te} resembling that of the circular cylinder to determine the flow regimes in the case of the hydrofoil in

Just Accepted

$$\mathrm{Re}_{te} = \frac{\rho h U_{te}}{\mu} \tag{13}$$

where h is the geometric thickness of the hydrofoil trailing edge, U_{te} is the time-averaged streamwise velocity at the hydrofoil trailing edge (x/c = 1.0), and ρ and μ are the density and dynamic viscosity of water, respectively. The values of Re_{te} under different slip lengths of 210 μm, 230 μm, 250 μm, and 500 μm are then calculated and demonstrated in Table 2.

Table 2 Validation of the bluntness effect under large slip lengths.

L_s (μm)	h (mm)	U_{te} (m/s)	Re_{te}	Flow phenomena in the present work	Flow regimes for circular cylinder [97, 98]
210	0.25	0.088	21.9	No vortex shedding	$\mathrm{Re} < \mathrm{Re}_{c1}$ ($\mathrm{Re}_{c1} \approx 49$) Two-dimensional steady regime
230	0.25	0.205	51.0	No vortex shedding	$\mathrm{Re} < \mathrm{Re}_{c1}$ ($\mathrm{Re}_{c1} \approx 49$) Two-dimensional steady regime
250	0.25	0.363	90.3	Two-dimensional like wake	$\mathrm{Re}_{c1} < \mathrm{Re} < \mathrm{Re}_{c2}$ ($\mathrm{Re}_{c1} \approx 49$, $\mathrm{Re}_{c2} \approx 140$–$194$) Two-dimensional unsteady regime
500	0.25	1.717	427.2	Three-dimensional turbulent wake	$260 < \mathrm{Re} < 1000$ Three-dimensional wake

It can be found from Table 2 that for the 210 μm slip case, Re_{te} = 21.9 falls well below the critical value $\mathrm{Re}_{c1} \approx 49$ for the onset of vortex shedding of a circular cylinder. For the 230 μm slip case, there is no obvious vortex shedding in the hydrofoil wake, and Re_{te} =51.0 for the hydrofoil is close to the critical value $\mathrm{Re}_{c1} \approx 49$ for the circular cylinder. Since Re_{te} is an effective Reynolds number constructed by analogy with the circular cylinder wake, the regime boundaries of the circular cylinder [97, 98] are used here as qualitative references rather than a strict criterion. Furthermore, there exists sharp corner at the hydrofoil trailing edge, which is significantly different from that of the circular cylinder. The fact that there is no obvious vortex shedding for the 230 μm slip case with Re_{te} =51.0 indicates that the critical Re range for the laminar vortex shedding of the hydrofoil may be slightly higher than that of the typical circular cylinder. For the 250 μm slip case, Re_{te} increases to 90.3, which is in the laminar vortex shedding regime as compared to the circular

Just Accepted

cylinder flow, and there indeed appears two-dimensional like vortex shedding in the hydrofoil wake. For the 500 μm slip case, Re_{te} is significantly increased, and there appears three-dimensional turbulent flow structures in the hydrofoil wake, which is consistent with the standard circular cylinder flow in the range of 260<Re<1000.

In addition, for the 500 μm slip case, the Strouhal number of the turbulent vortex shedding based on the tonal noise frequency (f = 1586 Hz) and the hydrofoil trailing edge thickness (h = 0.25 mm) is $St = fh/U_0 = 0.11$, which is consistent with the range of St = 0.08–0.11 for a flat plate with a blunt trailing edge [99, 100]. While for the 250 μm slip case, the corresponding St is about 0.04, which is lower than the typical value. Therefore, the vortex shedding for the 250 μm slip case has not been fully developed as that of the 500 μm case, which can be considered as a transitional state.

In summary, for moderate slip lengths of 50 μm, 100μm, and 180 μm, tonal peaks mainly originate from the periodic vortex shedding due to slip-induced flow separation bubbles or non-attached flow separation, giving rise to more pronounced tonal peaks. While for large slip lengths of 250 μm and 500 μm, tonal noise peaks originate from the periodic vortex shedding due to the slip-enhanced bluntness effect at the hydrofoil trailing edge.

4 Mechanisms of flow noise variation under surface slip

From the above results, the underlying mechanisms for the flow noise variation under the influence of surface slip can be illustrated, as shown in Fig. 16.

The flow evolution process can be divided into five regimes. In Regime I (No-slip case), laminar separation bubbles occur on the hydrofoil surface, and the instability of the laminar boundary layer can generate discrete tonal peaks in the SPL. In Regime II with small slip lengths (L_s = 10–20 μm), the instability of the boundary layer and flow separation bubbles are slightly weakened by surface slip, and the discrete tonal peaks are decreased compared to the no-slip case.

Just Accepted

In Regime III with moderate slip lengths (L_s = 50–180 μm), surface slip induces the occurrence of flow separation bubbles or non-attached flow separation on the hydrofoil surface, which results in periodic vortex shedding in the hydrofoil wake, and thereby gives rise to more pronounced tonal peaks. The OASPL is therefore increased for the 50 μm and 100 μm slip cases, while decreased for the 180 μm case due to the significantly low broadband noise level. In Regime IV with relatively large slip lengths (L_s = 210–230 μm), the hydrofoil surface is in full laminar state without flow separation, which demonstrates extremely low fluctuations. The broadband noise is therefore decreased, and the OASPL is the lowest. Finally, in Regime V with the largest slip lengths (L_s = 250–500 μm), the boundary layer over the hydrofoil surface remains fully laminar. However, the pronounced slip substantially reduces the boundary layer displacement thickness and enhances the bluntness effect. As a result, wake instability is triggered and prominent tonal peaks reappear, leading to an increase in the OASPL for the 500 μm slip case.

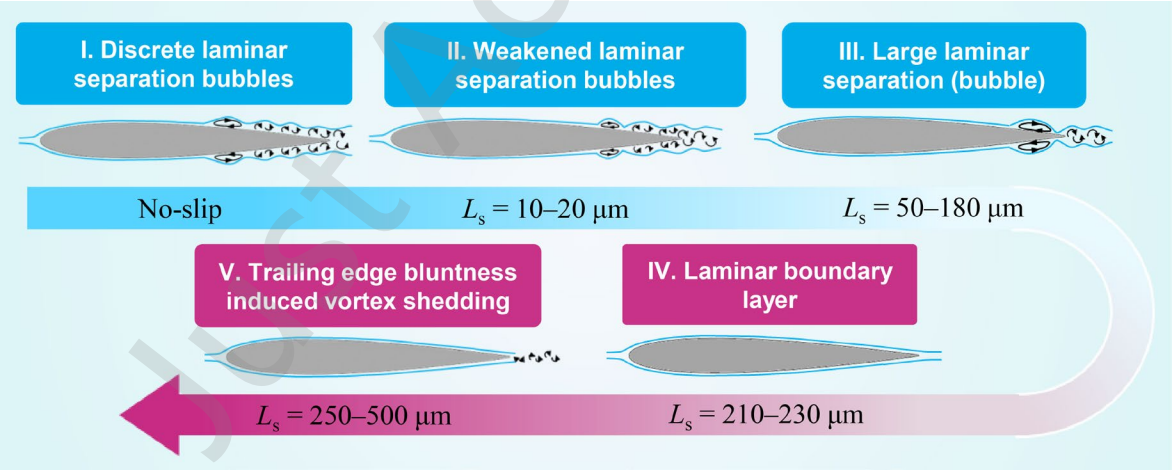


Figure 16 Flow field evolution under surface slip at zero angle of attack for the NACA 0012 hydrofoil.

Therefore, the hydrofoil noise characteristics exhibit discrete tonal peaks superimposed on the broadband hump at small slip lengths (10–20 μm), high tonal peaks due to large flow separation (bubbles) at moderate slip lengths (50–180 μm), extremely low broadband noise levels in laminar flow (210–230 μm), and finally the re-emergence of high tonal peaks associated with the enhanced

trailing edge bluntness effect at large slip lengths (250–500 μm). The variation of both the broadband and tonal noise under surface slip leads to the non-monotonic variation of the OASPL.

5 Conclusion

In the present work, the effects of surface slip on the flow noise characteristics of a NACA 0012 hydrofoil over a wide range of slip lengths (10–500 μm) at a moderate Reynolds number of $Re = 3.6\times10^5$ and zero angle of attack are systematically investigated using large eddy simulation (LES) coupled with the Ffowcs Williams–Hawkings (FW–H) acoustic analogy. A non-monotonic variation of the overall sound pressure level (OASPL) of the hydrofoil under slip effects has been found. Compared with the no-slip case, the OASPL is decreased at small slip lengths of 10–20 μm, increased at moderate slip lengths of 50–100 μm, decreased at large slip lengths of 180–250 μm, and increased again at the largest 500 μm slip lengths. It needs to be mentioned that although the OASPL is decreased for the 250 μm slip length, the tonal peaks are higher than that of the no-slip case, which still indicates a deteriorated flow noise performance for the 250 μm slip case.

The flow noise of the hydrofoil is found to be closely related to the flow field evolution under surface slip. Surface slip has been found to slightly weaken the discrete laminar separation bubbles and decrease the discrete tonal peaks for small slip lengths (10–20 μm), while it can induce stronger flow separation or large separation bubbles near the trailing edge which induces stronger tonal peaks at moderate slip lengths (50–180 μm). Subsequently, flow separation and transition are pushed away from the hydrofoil surface, demonstrating extremely low noise levels at the relatively large slips (210–230 μm). Finally, enhanced bluntness effect of the truncated trailing edge is induced at the largest slip lengths (250–500 μm), and high tonal peaks appear again. Due to the above flow field and noise sources evolution, the OASPL of the hydrofoil demonstrates a decrease–increase–decrease–increase non-monotonic variation.

Apart from the non-monotonic flow noise variation, it can be found that the hydrofoil drag

Just Accepted

exhibits a similar trend: it decreases slightly at first, then increases, and finally decreases substantially. These results indicate that surface slip can simultaneously reduce drag and mitigate noise. For the small and relatively large slip lengths (10–20 μm and 180–230 μm), drag reduction and noise mitigation occur concurrently. For the moderate slip lengths (50–100 μm), drag increase and noise increase occur simultaneously. For the largest slip lengths investigated in the present work (250–500 μm), however, a trade-off emerges between the drag reduction and noise mitigation. Although a large slip length yields substantial drag reduction, it does not necessarily suppress the flow noise. Therefore, the slip length should be carefully tailored to balance the hydrodynamic and hydroacoustic performances to benefit the overall performance. This work therefore offers valuable insights into the design and applications of slippery materials in practical conditions involving surface ships and underwater vehicles. In the future, more investigations on the slip effects at non-zero angles of attack, as well as experimental validation using practical slippery materials on hydrofoil surfaces, should be carried out to deepen the understanding of the underlying mechanisms.

Acknowledgements

Numerical simulations based on ANSYS Fluent were executed on the Sunway TaihuLight supercomputer at the National Supercomputer Center in Wuxi, China.

Author contribution statement

Manfu Zhu is responsible for Conceptualization, Data curation, Formal analysis, Investigation, Methodology, Software, Validation, Visualization, Writing - original draft, Writing - review & editing, Funding acquisition. Hongbo Huang is responsible for Formal analysis, Investigation, Validation, Writing - review & editing. Nan Zhang is responsible for Formal analysis, Investigation, Validation, Writing - review & editing. Weixi Huang is responsible for

Just Accepted

Formal analysis, Investigation, Methodology, Validation, Visualization, Funding acquisition, Writing - review & editing. Liran Ma is responsible for Conceptualization, Formal analysis, Funding acquisition, Resources, Supervision, Writing - review & editing. Jianbin Luo is responsible for Funding acquisition, Resources, Supervision. All the authors have approved the final manuscript.

Data availability

The data that support the findings of this study is available from the corresponding author upon reasonable request.

Declaration of competing interest

All the contributing authors report no conflicts of interest in this work.

Funding

The work is granted by the NSFC Excellence Research Group (No. 52488101), Fundamental and Interdisciplinary Disciplines Breakthrough Plan of the Ministry of Education of China (No. JYB2025XDXM209), NSFC projects (Nos. 12425206, 12272206), China Postdoctoral Science Foundation (2025M771400), and Shui Mu Tsinghua Scholar Program (2025SM032).

Use of AI statement

None.

Electronic Supplementary Material

Supplementary material (further details of the rod-airfoil configuration validation, mesh independence check for the NACA 0012 hydrofoil, hydrodynamics and sound pressure level variation of the hydrofoil, flow field for the hydrofoil under no-slip and slip conditions) is available in the online version of this article at https://doi.org/10.26599/OCEAN.2026.9470035.

Just Accepted

References

1. ADDIN EN.REFLIST 1. Pan, D.B., Xu, X.J., Liu, B.L., Xu, H.J., Wang, X.C., (2023). A review on drag reduction technology: Focusing on amphibious vehicles. *Ocean Eng.* 280, 114618. https://doi.org/10.1016/j.oceaneng.2023.114618.

2. Zhang, Y.Q., Su, C.W., Zou, Z.H., Li, J.Y., Ji, M.C., Song, X.Z., Li, J.F., Man, J., (2025). Underwater biomimetic structures and surface technologies: A frontier review from natural inspiration to engineering implementation. *Ocean Eng.* 334, 121591. https://doi.org/10.1016/j.oceaneng.2025.121591.

3. Zhu, F., Jiang, J.W., Xu, C.X., Huang, W.X., (2025). Numerical study on boundary layer flow over the bow of SUBOFF model with turbulent inflow. *J. Fluid Mech.* 1023, A10. https://doi.org/10.1017/jfm.2025.10820.

4. Zhu, M.F., Ma, L.R., Luo, J.B., (2024). L*-An index for evaluating long range performance of autonomous underwater vehicles (AUVs). *Friction* 12 (10), 2205-2221. https://doi.org/10.1007/s40544-023-0842-7.

5. Zhu, M.F., Ma, L.R., (2024). A review of recent advances in the effects of surface and interface properties on marine propellers. *Friction* 12 (2), 185-214. https://doi.org/10.1007/s40544-022-0716-4.

6. Liu, J.L., Hou, Y.Q., You, C.X., Zou, Y., Xiong, C.W., Shang, D.J., Lv, P.Y., Li, H.Y., Duan, H.L., (2025). Noise reduction measurement and biomimetic propeller optimization designs for unmanned underwater vehicles. *Exp. Fluids* 66 (4), 69. https://doi.org/10.1007/s00348-025-03995-1.

7. Liu, M., Ma, L.R., (2022). Drag reduction methods at solid-liquid interfaces. *Friction* 10 (4), 491-515. https://doi.org/10.1007/s40544-021-0502-8.

8. Ceccio, S.L., (2010). Friction drag reduction of external flows with bubble and gas injection. *Annu. Rev. Fluid Mech.* 42, 183-203. https://doi.org/10.1146/annurev-fluid-121108-145504.

9. Fukagata, K., Iwamoto, K., Hasegawa, Y., (2024). Turbulent drag reduction by streamwise traveling waves of wall-normal forcing. *Annu. Rev. Fluid Mech.* 56, 69-90. https://doi.org/10.1146/annurev-fluid-120720-021445.

10. Hu, Y.W., Sun, Y.K., Ma, L.R., Luo, J.B., (2025). A review of drag reduction methods and principles in bionic interface. *Friction* 13 (9), 9441033. https://doi.org/10.26599/frict.2025.9441033.

11. Osman, E., Xu, C.X., Huang, W.X., (2026). Experimental study of a zero-pressure-gradient turbulent boundary layer over a bioinspired surface with 3D-printed shark scales. *Phys. Fluids* 38 (1), 011901. https://doi.org/10.1063/5.0301233.

Just Accepted

12. Huang, Z.T., Zhu, S.C., Zhu, M.F., Tian, Y., Ma, L.R., (2025). A durable superhydrophobic surface with bud-particle structure prepared by one-step spray method. *Appl. Surf. Sci.* 679, 161255. https://doi.org/10.1016/j.apsusc.2024.161255.
13. Rothstein, J.P., (2010). Slip on superhydrophobic surfaces. *Annu. Rev. Fluid Mech.* 42, 89-109. https://doi.org/10.1146/annurev-fluid-121108-145558.
14. Tang, Z.Q., Tian, T.F., Molino, P.J., Skvortsov, A., Ruan, D., Ding, J., Li, Y.L., (2024). Recent advances in superhydrophobic materials development for maritime applications. *Adv. Sci.* 11 (16), 2308152. https://doi.org/10.1002/advs.202308152.
15. Huang, Z.T., Hu, Y.W., Liang, Z.X., Zhu, S.C., Ma, L.R., Luo, J.B., (2026). Spatially heterogeneous superwettability in groove surfaces: anchored plastron for underwater drag reduction. *Ocean*. https://doi.org/10.26599/OCEAN.2026.9470024.
16. Hardt, S., McHale, G., (2022). Flow and drop transport along liquid-infused surfaces. *Annu. Rev. Fluid Mech.* 54, 83-104. https://doi.org/10.1146/annurev-fluid-030121-113156.
17. Samaha, M.A., Gad-el-Hak, M., (2021). Slippery surfaces: A decade of progress. *Phys. Fluids* 33 (7), 071301. https://doi.org/10.1063/5.0056967.
18. Sang, X., Zhu, M.F., Sun, Y.K., Ma, L.R., (2025). Structural modulation of bioinspired slippery surface for enhanced underwater drag reduction. *Colloid Surf. A-Physicochem. Eng. Asp.* 727, 138303. https://doi.org/10.1016/j.colsurfa.2025.138303.
19. Ali, S.A.S., Azarpeyvand, M., da Silva, C.R.I., (2018). Trailing-edge flow and noise control using porous treatments. *J. Fluid Mech.* 850, 83-119. https://doi.org/10.1017/jfm.2018.430.
20. Ye, Q.Q., Zhu, Y.Z., Feng, Z.X., Lyu, B.S., Fan, Z.L., Song, Y.B., (2025). Trailing edge noise abatement of porous media with heterogeneous distribution. *Phys. Fluids* 37 (3), 035128. https://doi.org/10.1063/5.0256504.
21. Jaworski, J.W., Peake, N., (2020). Aeroacoustics of silent owl flight. *Annu. Rev. Fluid Mech.* 52, 395-420. https://doi.org/10.1146/annurev-fluid-010518-040436.
22. Li, S., Zhang, J., Chen, C., Huang, Z., (2026). Bio-inspired serrated hydrofoil: Vortex–pressure interactions and noise suppression mechanisms. *Phys. Fluids* 38 (1), 011902. https://doi.org/10.1063/5.0309132.
23. Lee, C., Choi, C.H., Kim, C.J., (2016). Superhydrophobic drag reduction in laminar flows: a critical review. *Exp. Fluids* 57 (12), 176. https://doi.org/10.1007/s00348-016-2264-z.
24. Park, H., Choi, C.H., Kim, C.J., (2021). Superhydrophobic drag reduction in turbulent flows: a critical review. *Exp. Fluids* 62 (11), 229. https://doi.org/10.1007/s00348-021-03322-4.
25. Singh, S.K., Narayanan, S., (2023). On the reductions of airfoil–turbulence noise by curved wavy serrations. *Phys. Fluids* 35 (7), 075140. https://doi.org/10.1063/5.0152637.

Just Accepted

26. Singh, S.K., Narayanan, S., (2023). Control of airfoil broadband noise through non-uniform sinusoidal trailing-edge serrations. *Phys. Fluids* 35 (2), 025139. https://doi.org/10.1063/5.0133556.

27. Wang, L., Liu, X., (2022). Aeroacoustic investigation of asymmetric oblique trailing-edge serrations enlighted by owl wings. *Phys. Fluids* 34 (1), 015113. https://doi.org/10.1063/5.0076272.

28. Navier, C.L.M.H., (1823). Mémoire sur les lois du mouvement des fluids. *Mem. Acad. R. Sci. Inst. Fr.* 6, 389-400.

29. Zhu, J.Y., Zhu, F.L., Su, W.D., Zou, S.F., Liu, L.Q., Shi, Y.P., Wu, J.Z., (2014). A vorticity dynamics view of "effective slip boundary" with application to foil-flow control. *Phys. Fluids* 26 (12), 123602. https://doi.org/10.1063/1.4904379.

30. Abu Rowin, W., Ghaemi, S., (2019). Streamwise and spanwise slip over a superhydrophobic surface. *J. Fluid Mech.* 870, 1127-1157. https://doi.org/10.1017/jfm.2019.225.

31. Lee, C., Choi, C.H., Kim, C.J., (2008). Structured surfaces for a giant liquid slip. *Phys. Rev. Lett.* 101 (6), 064501. https://doi.org/10.1103/PhysRevLett.101.064501.

32. Lee, C., Kim, C.J., (2009). Maximizing the giant liquid slip on superhydrophobic microstructures by nanostructuring their sidewalls. *Langmuir* 25 (21), 12812-12818. https://doi.org/10.1021/la901824d.

33. Martell, M.B., Perot, J.B., Rothstein, J.P., (2009). Direct numerical simulations of turbulent flows over superhydrophobic surfaces. *J. Fluid Mech.* 620, 31-41. https://doi.org/10.1017/s0022112008004916.

34. Martell, M.B., Rothstein, J.P., Perot, J.B., (2010). An analysis of superhydrophobic turbulent drag reduction mechanisms using direct numerical simulation. *Phys. Fluids* 22 (6), 065102. https://doi.org/10.1063/1.3432514.

35. Türk, S., Daschiel, G., Stroh, A., Hasegawa, Y., Frohnapfel, B., (2014). Turbulent flow over superhydrophobic surfaces with streamwise grooves. *J. Fluid Mech.* 747, 186-217. https://doi.org/10.1017/jfm.2014.137.

36. Seo, J., Mani, A., (2016). On the scaling of the slip velocity in turbulent flows over superhydrophobic surfaces. *Phys. Fluids* 28 (2), 025110. https://doi.org/10.1063/1.4941769.

37. Seo, J., García-Mayoral, R., Mani, A., (2018). Turbulent flows over superhydrophobic surfaces: flow-induced capillary waves, and robustness of air-water interfaces. *J. Fluid Mech.* 835, 45-85. https://doi.org/10.1017/jfm.2017.733.

38. Fairhall, C.T., Abderrahaman-Elena, N., García-Mayoral, R., (2019). The effect of slip and surface texture on turbulence over superhydrophobic surfaces. *J. Fluid Mech.* 861, 88-118. https://doi.org/10.1017/jfm.2018.909.

Just Accepted

39. Xie, W., Fairhall, C.T., Garcia-Mayoral, R., (2024). Resolving turbulence and drag over textured surfaces using texture-less simulations: the case of slip/no-slip textures. *J. Fluid Mech.* 1000, 35. https://doi.org/10.1017/jfm.2024.851.

40. Gogte, S., Vorobieff, P., Truesdell, R., Mammoli, A., van Swol, F., Shah, P., Brinker, C.J., (2005). Effective slip on textured superhydrophobic surfaces. *Phys. Fluids* 17 (5), 051701. https://doi.org/10.1063/1.1896405.

41. Lee, J., Kim, H., Park, H., (2018). Effects of superhydrophobic surfaces on the flow around an NACA0012 hydrofoil at low Reynolds numbers. *Exp. Fluids* 59 (7), 111. https://doi.org/10.1007/s00348-018-2564-6.

42. Sooraj, P., Jain, S., Agrawal, A., (2019). Flow over hydrofoils with varying hydrophobicity. *Exp Therm Fluid Sci* 102, 479-492. https://doi.org/10.1016/j.expthermflusci.2018.12.021.

43. Mallah, S.R., Sooraj, P., Sharma, A., Agrawal, A., (2021). Effect of superhydrophobicity on the wake of a pitching foil across various Strouhal numbers. *Phys. Fluids* 33 (11), 111905. https://doi.org/10.1063/5.0068088.

44. Liu, B., Feng, H.B., Yin, Z.C., Zhang, X., (2025). Numerical study of the natural transition in hydrofoil boundary layers with superhydrophobic surfaces. *Phys. Fluids* 37 (2), 024128. https://doi.org/10.1063/5.0257723.

45. Wang, K., Yang, L.M., Yu, Y., Hou, G.X., (2018). Influence of slip boundary on the hydrofoil with a curved slip boundary condition for the lattice Boltzmann method. *Phys. Fluids* 30 (12), 123601. https://doi.org/10.1063/1.5052323.

46. Peng, D., Xu, B.R., Yang, C.R., Liu, J.L., You, C.X., Yan, J.L., Gao, A.K., Lv, P.Y., Li, H.Y., (2026). Influence of local slip boundary condition on the hydrodynamic performance of hydrofoils for cross-domain vehicles at low Reynolds number. *Ocean Eng.* 343, 123342. https://doi.org/https://doi.org/10.1016/j.oceaneng.2025.123342.

47. Shahsavari, A., Nejat, A., Climent, E., Chini, S.F., (2023). Unexpected trends of lift for hydrofoils with superhydrophobic coating. *Eur. J. Mech. B-Fluids* 101, 219-226. https://doi.org/10.1016/j.euromechflu.2023.05.004.

48. Zhu, M.F., Huang, W.X., Ma, L.R., Luo, J.B., (2024). Influence of surface slip on hydrodynamics and flow field around a two-dimensional hydrofoil at a moderate Reynolds number. *Phys. Fluids* 36 (5), 055144. https://doi.org/10.1063/5.0203389.

49. Niu, C., Qin, Q.K., Liu, Y.W., Shang, D.J., Liu, W.B., (2023). Control effect of superhydrophobic grooves on flow-induced noise generated by flow around cylindrical shell at large Reynolds number. *Phys. Scr.* 98 (10), 105602. https://doi.org/10.1088/1402-4896/acf3b1.

Just Accepted

50. Barandagh, A.R., Ghazanfarian, J., (2024). Hydroacoustics of turbulent flow over superhydrophobic and oscillating cylinders. *Ocean Eng.* 294, 116751. https://doi.org/10.1016/j.oceaneng.2024.116751.
51. Chen, N., Yongwei, L., Dejiang, S., Qikai, Q., Wenbo, L., (2022). Hydrodynamic noise reduction mechanism of a superhydrophobic surface with different slip velocities. *J. Sound Vibr.* 531, 116976. https://doi.org/10.1016/j.jsv.2022.116976.
52. Lissaman, P.B.S., (1983). Low-Reynolds-number airfoils. *Annu. Rev. Fluid Mech.* 15, 223-239. https://doi.org/10.1146/annurev.fl.15.010183.001255.
53. Mueller, T.J., DeLaurier, J.D., (2003). Aerodynamics of small vehicles. *Annu. Rev. Fluid Mech.* 35, 89-111. https://doi.org/10.1146/annurev.fluid.35.101101.161102.
54. Wang, S., Zhou, Y., Alam, M.M., Yang, H., (2014). Turbulent intensity and Reynolds number effects on an airfoil at low Reynolds numbers. *Phys. Fluids* 26 (11). https://doi.org/10.1063/1.4901969.
55. Tam, C.K.W., Ju, H., (2012). Aerofoil tones at moderate Reynolds number. *J. Fluid Mech.* 690, 536-570. https://doi.org/10.1017/jfm.2011.465.
56. Pröbsting, S., Serpieri, J., Scarano, F., (2014). Experimental investigation of aerofoil tonal noise generation. *J. Fluid Mech.* 747, 656-687. https://doi.org/10.1017/jfm.2014.156.
57. Pröbsting, S., Scarano, F., Morris, S.C., (2015). Regimes of tonal noise on an airfoil at moderate Reynolds number. *J. Fluid Mech.* 780, 407-438. https://doi.org/10.1017/jfm.2015.475.
58. Arcondoulis, E., Doolan, C.J., Zander, A.C., Brooks, L.A., Liu, Y., (2019). An investigation of airfoil dual acoustic feedback mechanisms at low-to-moderate Reynolds number. *J. Sound Vibr.* 460, 114887. https://doi.org/https://doi.org/10.1016/j.jsv.2019.114887.
59. Desquesnes, G., Terracol, M., Sagaut, P., (2007). Numerical investigation of the tone noise mechanism over laminar airfoils. *J. Fluid Mech.* 591, 155-182. https://doi.org/10.1017/S0022112007007896.
60. Lowson, M., Fiddes, S., Nash, E., Laminar boundary layer aero-acoustic instabilities, 32nd Aerospace Sciences Meeting and Exhibit.
61. Sandberg, R.D., Jones, L.E., Sandham, N.D., Joseph, P.F., (2009). Direct numerical simulations of tonal noise generated by laminar flow past airfoils. *J. Sound Vibr.* 320 (4), 838-858. https://doi.org/https://doi.org/10.1016/j.jsv.2008.09.003.
62. Nicoud, F., Ducros, F., (1999). Subgrid-scale stress modelling based on the square of the velocity gradient tensor. *Flow Turbul. Combust.* 62 (3), 183-200. https://doi.org/10.1023/a:1009995426001.
63. Williams, J.E., Hawkings, D.L., (1969). Sound generation by turbulence and surfaces in arbitrary motion. *Philosophical Transactions of the Royal Society of London Series a-*

Just Accepted

Mathematical and Physical Sciences 264 (1151), 321-342. https://doi.org/10.1098/rsta.1969.0031.

64. Sezen, S., Cosgun, T., Yurtseven, A., Atlar, M., (2021). Numerical investigation of marine propeller inderwater radiated noise using acoustic analogy part 1: The influence of grid resolution. *Ocean Eng.* 220, 108448. https://doi.org/10.1016/j.oceaneng.2020.108448.

65. Chen, L.F., Jia, X.L., Xu, P., Chen, D.Y., Yang, K.D., Wang, J.L., Dong, Y.H., Wu, J.F., Zhou, F.C., (2026). Hydroacoustic reduction mechanism for the bionic hydrofoil. *Phys. Fluids* 38 (3), 037106. https://doi.org/10.1063/5.0311673.

66. Liu, L.Y., Li, W.P., (2026). Nonlinear wake noise of an underwater propeller under nonuniform inflow. *Phys. Fluids* 38 (5), 056108. https://doi.org/10.1063/5.0313521.

67. Wu, J.F., Yangzhou, J., Ma, Z.K., Huang, X., (2023). Numerical study of rotor unsteady forces and noise due to ingestion of grid-generated turbulence. *Phys. Fluids* 35 (1), 015141. https://doi.org/10.1063/5.0132975.

68. Lighthill, M.J., (1952). On sound generated aerodynamically I. General theory. *Proceedings of the Royal Society of London. A. Mathematical and Physical Sciences* 211 (1107), 564-587. https://doi.org/10.1098/rspa.1952.0060.

69. Lighthill, M.J., (1954). On sound generated aerodynamically II. Turbulence as a source of sound. *Proceedings of the Royal Society of London. A. Mathematical and Physical Sciences* 222 (1148), 1-32. https://doi.org/10.1098/rspa.1954.0049.

70. Blake, W.K., (2017). Mechanics of flow-induced sound and vibration. Volume 1: General concepts and elementary sources. Second Edition ed. UK: Academic Press, Elsevier.

71. Jacob, M.C., Boudet, J., Casalino, D., Michard, M., (2005). A rod-airfoil experiment as a benchmark for broadband noise modeling. *Theor. Comput. Fluid Dyn.* 19 (3), 171-196. https://doi.org/10.1007/s00162-004-0108-6.

72. Qin, D.H., Pan, G., Lee, S., Huang, Q.G., Shi, Y., (2019). Underwater radiated noise reduction technology using sawtooth duct for pumpjet propulsor. *Ocean Eng.* 188, 106228. https://doi.org/10.1016/j.oceaneng.2019.106228.

73. Zhang, N., Xie, H., Wang, X., Wu, B.S., (2016). Computation of vortical flow and flow induced noise by large eddy simulation with FW-H acoustic analogy and Powell vortex sound theory. *J. Hydrodyn.* 28 (2), 255-266. https://doi.org/10.1016/s1001-6058(16)60627-3.

74. Zhang, N., Wang, X., Xie, H., Li, Y., (2016). Research on numerical simulation approach for flow induced noise and the influence of the acoustic integral surface. *Journal of Ship Mechanics* 20 (7), 892-908.

75. Gelot, M.B.R., Kim, J.W., (2020). Effect of serrated trailing edges on aerofoil tonal noise. *J. Fluid Mech.* 904, A30. https://doi.org/10.1017/jfm.2020.724.

Just Accepted

76. Romani, G., Casalino, D., van der Velden, W., (2021). Numerical analysis of airfoil trailing-edge noise for straight and serrated edges at incidence. *AIAA J.* 59 (7), 2558-2577. https://doi.org/10.2514/1.J059457.

77. Yang, C.H., Liu, Y., Zhang, X.Z., Bi, C.X., (2024). Hybrid control of aerofoil self-noise by coupling air blowing and trailing-edge serration. *J. Sound Vibr.* 575, 118265. https://doi.org/10.1016/j.jsv.2024.118265.

78. Hu, Y.S., Zhang, P.J.Y., Wan, Z.H., Liu, N.S., Sun, D.J., Lu, X.Y., (2022). Effects of trailing-edge serration shape on airfoil noise reduction with zero incidence angle. *Phys. Fluids* 34 (10), 105108. https://doi.org/10.1063/5.0108565.

79. Jones, L.E., Sandberg, R.D., (2012). Acoustic and hydrodynamic analysis of the flow around an aerofoil with trailing-edge serrations. *J. Fluid Mech.* 706, 295-322. https://doi.org/10.1017/jfm.2012.254.

80. Wang, L., Liu, X.M., Li, D., (2021). Noise reduction mechanism of airfoils with leading-edge serrations and surface ridges inspired by owl wings. *Phys. Fluids* 33 (1), 17. https://doi.org/10.1063/5.0035544.

81. Wang, X.C., Song, M.T., Lin, C., Yang, Z.P., Cheng, H.Y., Ji, B., (2026). Numerical investigation of hydrofoil cloud cavitation noise in a confined domain. *Ocean Eng.* 357, 12. https://doi.org/10.1016/j.oceaneng.2026.125655.

82. Bose, S.T., Park, G.I., (2018). Wall-modeled large-eddy simulation for complex turbulent flows. *Annu. Rev. Fluid Mech.* 50, 535-561. https://doi.org/10.1146/annurev-fluid-122316-045241.

83. Sheldahl, R.E., Klimas, P.C., (1981). Aerodynamic characteristics of seven symmetrical airfoil sections through 180-degree angle of attack for use in aerodynamic analysis of vertical axis wind turbines. Albuquerque: Sandia National Laboratories.

84. Georgiadis, N.J., Rizzetta, D.P., Fureby, C., (2010). Large-eddy simulation: Current capabilities, recommended practices, and future research. *AIAA J.* 48 (8), 1772-1784. https://doi.org/10.2514/1.J050232.

85. Wang, X.C., Cheng, H.Y., Ji, B., (2026). Bursting of wetted and cavitating tip vortex around a wake-influenced propeller. *Phys. Rev. Fluids* 11 (1), 28. https://doi.org/10.1103/rt5v-1nk3.

86. Arbey, H., Bataille, J., (1983). Noise generated by airfoil profiles placed in a uniform laminar flow. *J. Fluid Mech.* 134, 33-47. https://doi.org/10.1017/S0022112083003201.

87. Liu, B., Liu, J.H., Zhang, Y.M., (2024). Numerical investigation of the natural transition in boundary layers on underwater axisymmetric bodies with superhydrophobic surfaces. *Phys. Fluids* 36 (1), 014124. https://doi.org/10.1063/5.0175594.

Just Accepted

88. Liu, B., Zhang, Y.M., (2020). A numerical study on the natural transition locations in the flat-plate boundary layers on superhydrophobic surfaces. *Phys. Fluids* 32 (12), 124103. https://doi.org/10.1063/5.0030713.

89. Chen, J.D., Gao, A.K., Yao, Y., Zhang, G.B., Chen, S.H., (2026). Drag reduction of SUBOFF model with deep-learning-optimized distributed partial-slip boundaries. *Phys. Fluids* 38 (4), 16. https://doi.org/10.1063/5.0317603.

90. Min, T., Kim, J., (2004). Effects of hydrophobic surface on skin-friction drag. *Phys. Fluids* 16 (7), L55-L58. https://doi.org/10.1063/1.1755723.

91. Min, T., Kim, J., (2005). Effects of hydrophobic surface on stability and transition. *Phys. Fluids* 17 (10), 108106. https://doi.org/10.1063/1.2126569.

92. Li, H.Y., Ji, S.S., Tan, X.K., Li, Z.X., Xiang, Y.L., Lv, P.Y., Duan, H.L., (2020). Effect of Reynolds number on drag reduction in turbulent boundary layer flow over liquid-gas interface. *Phys. Fluids* 32 (12). https://doi.org/10.1063/5.0027727.

93. Jones, L.E., Sandberg, R.D., (2011). Numerical analysis of tonal airfoil self-noise and acoustic feedback-loops. *J. Sound Vibr.* 330 (25), 6137-6152. https://doi.org/https://doi.org/10.1016/j.jsv.2011.07.009.

94. Mele, B., Tognaccini, R., (2018). Slip length-based boundary condition for modeling drag reduction devices. *AIAA J.* 56 (9), 3478-3490. https://doi.org/10.2514/1.J056589.

95. Mele, B., Tognaccini, R., Catalano, P., de Rosa, D., (2020). Effect of body shape on riblets performance. *Phys. Rev. Fluids* 5 (12), 124609. https://doi.org/10.1103/PhysRevFluids.5.124609.

96. Lu, Z., Zhang, F., Jin, F., Xiao, R., Tao, R., (2022). Influence of the hydrofoil trailing-edge shape on the temporal-spatial features of vortex shedding. *Ocean Eng.* 246, 110645. https://doi.org/https://doi.org/10.1016/j.oceaneng.2022.110645.

97. Derakhshandeh, J.F., Alam, M.M., (2019). A review of bluff body wakes. *Ocean Eng.* 182, 475-488. https://doi.org/10.1016/j.oceaneng.2019.04.093.

98. Williamson, C.H.K., (1996). Vortex dynamics in the cylinder wake. *Annu. Rev. Fluid Mech.* 28, 477-539. https://doi.org/10.1146/annurev.fl.28.010196.002401.

99. Herr, M., Dobrzynski, W., (2005). Experimental investigations in low-noise trailing-edge design. *AIAA J.* 43 (6), 1167-1175. https://doi.org/10.2514/1.11101.

100. Moreau, D.J., Doolan, C.J., (2013). Noise-reduction mechanism of a flat-plate serrated trailing edge. *AIAA J.* 51 (10), 2513-2522. https://doi.org/10.2514/1.J052436.

Just Accepted